Department of Physics and Astronomy

University of Heidelberg

Master thesis

in Physics

submitted by

Stefan Erlewein

born in Stuttgart

2017

Trapping of gold anions in a linear Paul trap

This Master thesis has been carried out by Stefan Erlewein

at the

Max Planck Institute for Nuclear Physics

under the supervision of

Herrn Priv.-Doz. Dr. Alban Kellerbauer

Einfang von Gold-Anionen in einer linearen Paul-Falle:

Um die Möglichkeit von Laserkühlung an negativ geladenen Ionen zu demonstrieren ist es notwendig, die Ionen in einer Umgebung frei von starken Magnetfeldern einzuschließen. Im Zuge dieser Arbeit wurde der bestehende Entwurf einer linearen Paul-Falle modifiziert und in Betrieb genommen. Der neue Entwurf verfügt über zwei zusätzliche Endkappen-Elektroden deren Form einen effektiven Einschluss in axialer Richtung ermöglicht, ohne den optischen Zugang zu blockieren. Der Einfluss dieser Elektroden auf das Fallenpotential wurde simuliert und mit den experimentellen Ergebnissen verglichen. Untersuchungen mit AU^--Ionen zeigen, dass die Falle das Speichern von Ionen über mehrere Stunden erlaubt. Messungen der Speicherzeit deuten darauf hin, dass der Ladeprozess die gespeicherten Ionen aufheizt. Die experimentell bestimmte Lebensdauer τ_{Hot} der aufgeheizten Ionen beträgt $23(3)$ min und erhöht sich nach Abkühlung auf $75(2)$ min. Durch Messungen des Radius des gespeicherten Ionenplasmas wurde eine Abschätzung der Gleichgewichtstemperatur $T_\infty \approx 5000\,\mathrm{K}$ ermittelt. Die auf gleiche Weise experimentell bestimmte Zeitkonstante des Kühlprozesses beträgt $\tau_{Cool} = 41.6(4)\,\mathrm{s}$.

Trapping of gold anions in a linear Paul trap:

In order to demonstrate laser cooling on negatively charged ions, it is necessary to confine the ions in a region free of strong magnetic fields. In the course of this thesis, the pre-existing design of a linear Paul trap was modified and taken into operation. The new design possesses two additional end cap electrodes whose shape provides effective axial confinement without blocking optical access to the trapped particles. The influence of these end cap electrodes on the trapping potential was simulated and compared to experimental results. Measurements with $\{textAU^-$ ions show that the trap allows storage of ions for multiple hours. Analysis of the storage time suggests that the loading process heats up the trapped ions. The lifetime τ_{Hot} of the hot ions was determined to be $23(3)$ min. After thermalization, the lifetime increases to $75(2)$ min. Measurements of the ion cloud's radius provide an estimation of the equilibrium temperature $T_\infty \approx 5000\,\mathrm{K}$. The experimentally determined time constant of the cooling process is $\tau_{Cool} = 41.6(4)\,\mathrm{s}$.

Contents

1 Introduction

1.1 Motivation

Ions play an important role in various fields of science, ranging from Biology and Medicine [1] to Chemistry, Physics and Astronomy [2]. Positive ions can be created by removing electrons from a neutral atom. Nowadays it is possible to create highly charged ions up to ^{+92}U, allowing to perform precision experiments under extreme conditions [3]. As far as negative ions are concerned, so far only singly charged atomic ions have been found [4], as the additional electron is bound by weak polarization and correlation effects between the overlapping wave functions of all bound electrons.

Conducting precision experiments in atomic physics often requires the ions or particles to be cold. If an ion species exhibits a suitable transition, its temperature can be decreased via laser cooling. Even if no such transition exists, the desired ions of species A can be cooled by trapping them together with cooled particles of another species B. This cooling scheme is called sympathetic cooling. While laser cooling of positive ions and neutral atoms nowadays is a well established technique, laser cooling of negative ions has so far never been demonstrated.

One of the most intriguing prospects of direct laser cooling of negative ions is the possibility to sympathetically cool antiprotons [5]. As antiprotons are negatively chargeed, the species of particles used to cool them sympathetically has to have negative charge as well. Trying to use neutral or positive particles would result in annihilation as soon as the antiprotons come into contact with them. By using negative ions, the Coulomb barrier reduces the annihilation cross section significantly, thus allowing storage of matter and antimatter in a common trap. The availability of cold antiprotons leads to the possibility of creating cold antihydrogen via a charge exchange reaction which opens the door to new precision measurements investigating the symmetries between matter and antimatter. Other approaches for the creation of cold antihydrogen include evaporative cooling [6] and sympathetic cooling of $\overline{\mathrm{H}}^+$ [7]. While there have been proposals to create cold antihydrogen by sympathetically cooling antiprotons with an electron plasma coupled to a dilution refrigerator [8], this would limit the attainable temperature to $\approx$100 mK. Our group is trying to demonstrate the feasibility of direct laser cooling of negative atomic ions.

While a large number of elements can form negative ions [9], most of these ions posses a small electron affinity, which means that the additional electron is weakly bound. Trying to excite a transition in such an ion usually leads to dissociation into a neutral atom and an electron. Osmium, cerium and lanthanum are the only known elements whose negative ions exhibit a transition between bound states of opposite parity, which is necessary for efficient laser cooling. The suitability of these ions for laser cooling, however, varies a lot. The following paragraph summarizes the information presented in [10] and [11].

Osmium was the first of the three elements mentioned above for which such a bound-bound transition was detected experimentally [12], making Os^- a candidate for laser cooling. High resolution spectroscopy performed at the Max Planck Institute for Nuclear Physics in 2009 [13] showed, however, that the lifetime of the excited state was larger than first believed, which caused the expected cooling time to be unfeasibly long.
Cerium, while having bound transitions, is not suitable for laser cooling as both dipole transitions that were discovered by Walter et al. in 2011 [14] are spin-forbidden. At the same time, Ce^- has several dark states which further complicates the realization of a potential cooling scheme.
Lanthanum, the third of the possible candidates mentioned above, nowadays seems to be the most promising candidate for laser cooling of negative ions. The bound-bound transition predicted in 1991 by Vosko et al. [15] was first detected by Covington et al. in 1998 [16]. Relativistic configuration-interaction calculations performed by O'Malley and Beck [17] predicted the lifetime of the excited state to be $\tau = 34\,\mu s$ with a branching ratio for decay into the transition's ground state over 99.98 %, which means that cooling without repumping might be feasible.

The time the ions have to be cooled to reach low temperatures has to be multiple times larger than the transition's lifetime. As the source producing La^- creates the ions at high velocities, the interaction time between a laser and the ion beam is short compared to the required cooling time. In order to increase the interaction time between the cooling laser and the La^- ions, it is necessary to trap the ions in a region free from strong magnetic fields. The absence of magnetic fields is required to avoid complicating the level structure of La^- by Zeeman splitting. In the course of this thesis, the preexisting design of a Paul trap providing such confinement was modified, simulated, assembled and tested.

1.2 Trapping of charged particles

In order to cool negative ions, it is necessary to confine the ions to a small volume. The ideal particle trap would confine an ion to a single point in space. In the case of positively charged ions this means that the electrostatic potential $U(x, y, z)$ confining the particle has to have a minimum in this point. Samuel Earnshaw proved in 1842 that such a point can not exist in charge-free space [18]. For such a trapping to be stable the electric field $E = -\nabla U$has to vanish in this point while the 2nd partial derivatives $\frac{\partial^2 U}{\partial x^2}$, $\frac{\partial^2 U}{\partial y^2}$ and $\frac{\partial^2 U}{\partial z^2}$ have to be positive. While it is possible for the electric field to vanish, the Laplace equation

$$\Delta U = \frac{\partial^2 U}{\partial x^2} + \frac{\partial^2 U}{\partial y^2} + \frac{\partial^2 U}{\partial z^2} = 0 \tag{1.1}$$

states that the divergence of the field has to be zero, thus rendering the above mentioned requirement impossible. The same is the case for negative ions, as for negative charges to be stably trapped in a point all second derivatives would have to be negative.

To overcome this problem, two different approaches have been developed over time: Paul traps use an alternating electric field to achieve stable confinement while Penning traps combine static electric and magnetic fields.

1.2.1 The ideal Penning Trap

Penning traps use a combination of an static electric and magnetic fields to confine charged particles in all spatial dimensions. After the first systematic experiments of particle movement in a combined magneto- and electrostatic field by Dutch physicist Frans Michel Penning [19] in 1936 it took another 20 years until Hans Georg Dehmelt built the first trap of this type. Brown and Gabrielse later performed a systematic analysis and found several important theorems linking the characteristic frequencies [20].

To see why this field configuration traps particles, we derive the equations of motion for a single charged particle of mass m and charge Q. Trapping along the z-axis is achieved by two hyperbolic end cap electrodes and one hyperbolic ring electrode. This electrode configuration creates a harmonic potential on the z-axis which, in order to satisfy the Laplace equation, has to be repelling in radial direction r. Figure 1.1 shows the potential dependence on the z-axis and the $z = 0$ plane. Given the voltage difference U_0 between the end cap electrodes and the ring electrode the electrostatic potential U can be written as

$$U = U_0 \frac{z^2 - \frac{r^2}{2}}{2d^2} = U_0 \frac{z^2 - \frac{x^2+y^2}{2}}{2d^2} \qquad \text{with } d = \sqrt{\frac{z_0^2 + \frac{r_0^2}{2}}{2}}. \tag{1.2}$$

The parameter d is determined by the electrodes' respective minimum distances z_0 and r_0 from the trap center.

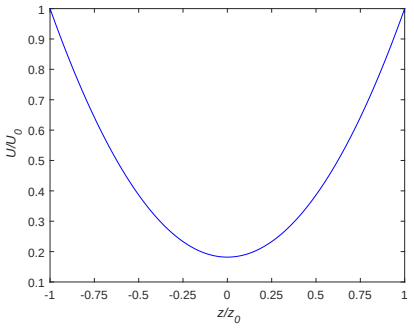

(a) Potential along the z-axis for $r = 0$

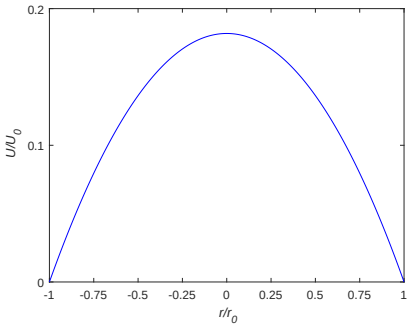

(b) Potential along the radial direction for $z = 0$

Figure 1.1: Electrostatic potential in an ideal Penning trap for $\frac{z_0}{r_0} = \frac{3}{2}$

To counteract the potential's repelling part, a homogenous magnetic field B pointing in the z-direction is superimposed.

$$\vec{B} = B_0 \vec{e}_z \tag{1.3}$$

A particle of mass m and charge Q moving with velocity $\vec{v}$ in these fields experiences the force

$$\vec{F} = \vec{F}_E + \vec{F}_B = Q(\vec{E} + \vec{v} \times \vec{B}) = Q(-\nabla U + \vec{v} \times \vec{B}). \tag{1.4}$$

Using this relationship, we can determine the equations of motion for every component and receive

$$\ddot{x} = \frac{Q}{m}(\frac{U_0}{2d^2}x + B_0\dot{y}) = \frac{1}{2}\omega_z^2 x + \omega_C \dot{y} \tag{1.5}$$

$$\ddot{y} = \frac{Q}{m}(\frac{U_0}{2d^2}y - B_0\dot{x}) = \frac{1}{2}\omega_z^2 y - \omega_C \dot{x} \tag{1.6}$$

$$\ddot{z} = -\frac{Q}{m}\frac{U_0}{d^2}z = -\omega_z^2 z \tag{1.7}$$

with the frequencies $\omega_z = \frac{QU_0}{2md^2}$ called axial frequency and $\omega_C = \frac{QB_0}{m}$ called free cyclotron frequency.

The motion in z-direction is decoupled from the radial motion and is be solved by a harmonic oscillation with the axial frequency:

$$z(t) = R_z \cos(\omega_z t + \varphi_z). \tag{1.8}$$

The amplitude R_z and the phase φ_z depend on the initial conditions.

To solve the equations of motion in radial direction we introduce the complex variable $u = x + \mathrm{i}y$ [21]. This lets us describe the motion in x- and y-direction with one equation:

$$\ddot{u} = \frac{1}{2}\omega_z^2 - \mathrm{i}\omega_C \dot{u}. \tag{1.9}$$

Using the common ansatz $u(t) = Re^{-\mathrm{i}\omega t + \varphi}$ for linear differential equations, 1.9 reduces to

$$\omega^2 - \omega_C \omega + \frac{1}{2}\omega_z^2 = 0 \tag{1.10}$$

This equation is solved by the modified cyclotron frequency

$$\omega_+ = \frac{1}{2}\left(\omega_C + \sqrt{\omega_C^2 - 2\omega_z^2}\right) \tag{1.11}$$

and the magnetron frequency

$$\omega_- = \frac{1}{2}\left(\omega_C - \sqrt{\omega_C^2 - 2\omega_z^2}\right). \tag{1.12}$$

These motions will only be bounded if the root $\sqrt{\omega_C^2 - 2\omega_z^2}$ is real, thus placing a constraint on the minimum magnetic field B_{min} required for trapping:

$$B_{min}^2 = \frac{4U_0 m}{d^2 Q}, \tag{1.13}$$

with $U_0 Q > 0$ required for axial trapping. From Eq 1.13 it becomes obvious that for a given magnetic field B all particles with a charge to mass ratio $\frac{Q}{m} > \frac{4U_0}{d^2 B}$ can be trapped, which allows storing of particles of vastly different masses in a common trap.
Putting the solutions from Eqs 1.11 and 1.12 back into the ansatz allows us to choose R_+,R_-,φ_+ and φ_-. Separating the real and the imaginary part of the solution leads to the following equations for the radial motion in the trap:

$$x(t) = R_+ \cos(\omega_+ t + \varphi_+) + R_- \cos(\omega_- t + \varphi_-) \tag{1.14}$$

$$y(t) = -\frac{Q}{|Q|}(R_+ \sin(\omega_+ t + \varphi_+) + R_- \sin(\omega_- t + \varphi_-)) \tag{1.15}$$

Figure 1.2 depicts the different eigenmotions in all dimensions. Note that the radii and frequencies were chosen in a way that allows clear visibility and are not to scale.

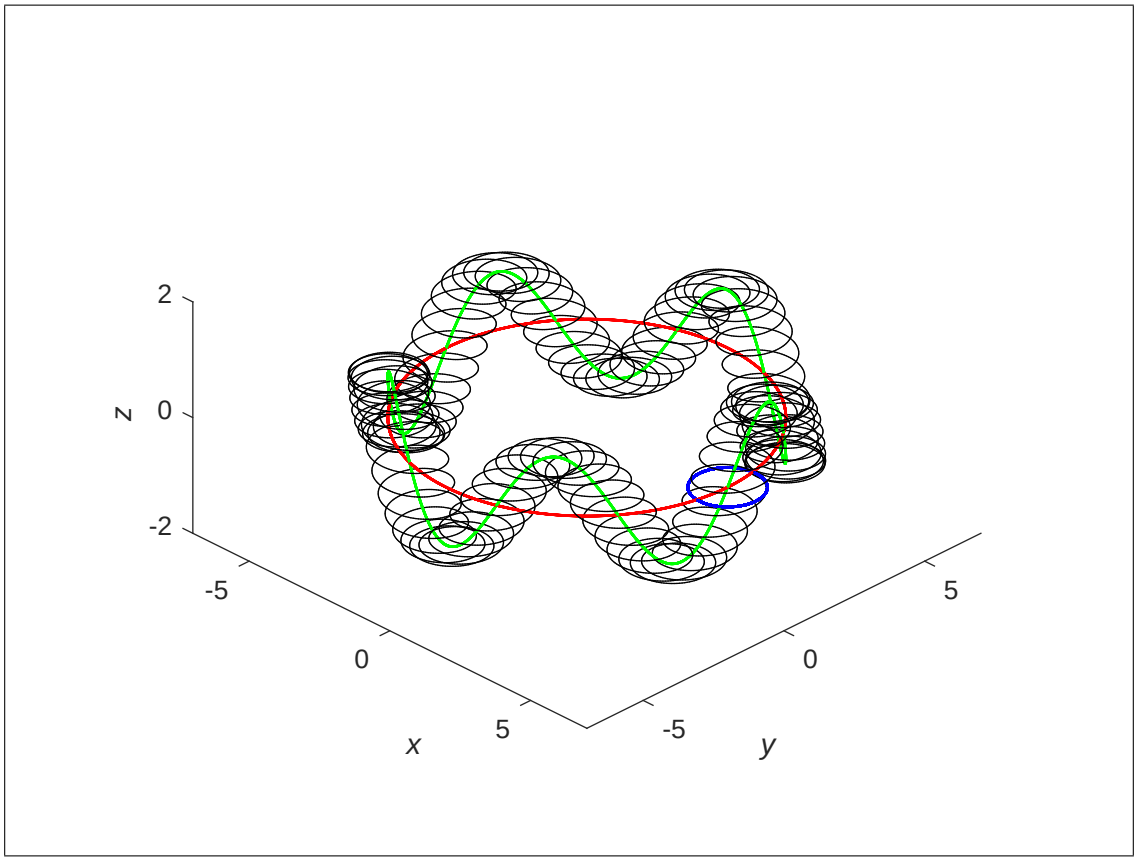

Figure 1.2: Red: Magnetron motion. Blue: Cyclotron Motion. Green: Magnetron motion and axial motion. Black: Motion of a particle in a Penning trap

1.2.2 The ideal Paul Trap

In contrast to Penning traps, the confinement in Paul traps is realized by a combination of static and alternating electric potentials. This has the advantage that it is not necessary to create a magnetic field. The idea behind the Paul trap was first described by Paul and Steinwedel [22] in 1953 who suggested to use a combination of electrostatic and electrodynamic fields acting as a mass spectrometer. The trajectory of a particle passing such a field either stays bound or increases exponentially with time, depending on the particle's charge-to-mass ratio. This principle can be used to trap particles by using the ponderomotive force created by the alternating potential. To determine the conditions necessary for trapping a particle of mass m and charge Q, we follow the description by Werth [21].

Ideal Paul traps use the same electrode configuration as Penning traps. Two hyperbolic end cap electrodes and a hyperbolic ring electrode create a time-varying quadrupole potential. In contrast to the Penning trap the voltage applied between the end caps and the ring electrode contains both DC and AC components, which creates a time dependent potential

$$U(t) = U_0(t)\frac{z^2 - \frac{r^2}{2}}{2d^2} = (U_{DC} + U_{AC}\cos(\Omega t))\frac{z^2 - \frac{x^2+y^2}{2}}{2d^2} \qquad \text{with } d = \sqrt{\frac{z_0^2 + \frac{r_0^2}{2}}{2}} \tag{1.16}$$

The parameter d once again is being determined by the electrodes' respective minimum distances z_0 and r_0 from the trap center. Proceeding the same way we did for the Penning trap, we determine the particle's equations of motion and get

$$\ddot{x} = \frac{Q}{m}\frac{U_{DC} + U_{AC}\cos(\Omega t)}{2d^2}x \tag{1.17}$$

$$\ddot{y} = \frac{Q}{m}\frac{U_{DC} + U_{AC}\cos(\Omega t)}{2d^2}y \tag{1.18}$$

$$\ddot{z} = -\frac{Q}{m}\frac{U_{DC} + U_{AC}\cos(\Omega t)}{d^2}z. \tag{1.19}$$

By applying the substitutions

$$\begin{aligned} a_x = a_y &= -\frac{2QU_{DC}}{md^2\Omega^2} & q_x = q_y &= \frac{QU_{AC}}{md^2\Omega^2} \\ a_z &= \frac{4QU_{DC}}{md^2\Omega^2} & q_z &= \frac{2QU_{AC}}{md^2\Omega^2} \\ \text{and } \tau &= \frac{1}{2}\Omega t \end{aligned}$$

these equations can be transformed into the Mathieu equation:

$$\frac{\mathrm{d}^2 u_j}{\mathrm{d}\tau^2} + (a_j + 2q_j\cos(2\tau))u_j = 0 \qquad \text{for } j = x, y, z \tag{1.20}$$

While this equation is difficult to solve, Floquet's theorem states that the solutions are of the form

$$u_1(\tau) = e^{(\alpha+\mathrm{i}\beta)\tau}\Phi(\tau) \qquad \text{and} \qquad u_2(\tau) = e^{-(\alpha+\mathrm{i}\beta)\tau}\Phi(-\tau), \tag{1.21}$$

with $\Phi(\tau)$ being a π-periodic function and α and β being real-valued functions of the parameters a and q. According to Werth [21], the general solution is only bound if $\alpha = 0$ and $\beta \notin \mathbb{Z}$. β can be calculated from the parameters a and q using a continued fraction:

$$\beta^2 = a + f(\beta) + f(-\beta) \tag{1.22}$$

$$\text{with } f(\beta) = \frac{q^2}{(2+\beta)^2 - a - \frac{q^2}{(4+\beta)^2 - a - \ldots}}. \tag{1.23}$$

This allows us to separate into regions where the solution stays bound and regions where it diverges. The border between stable and unstable regions is given by the values of a and q for which $\beta(a, q) \in \mathbb{N}$. Figure 1.3 shows the first stability regions in a-q-space.

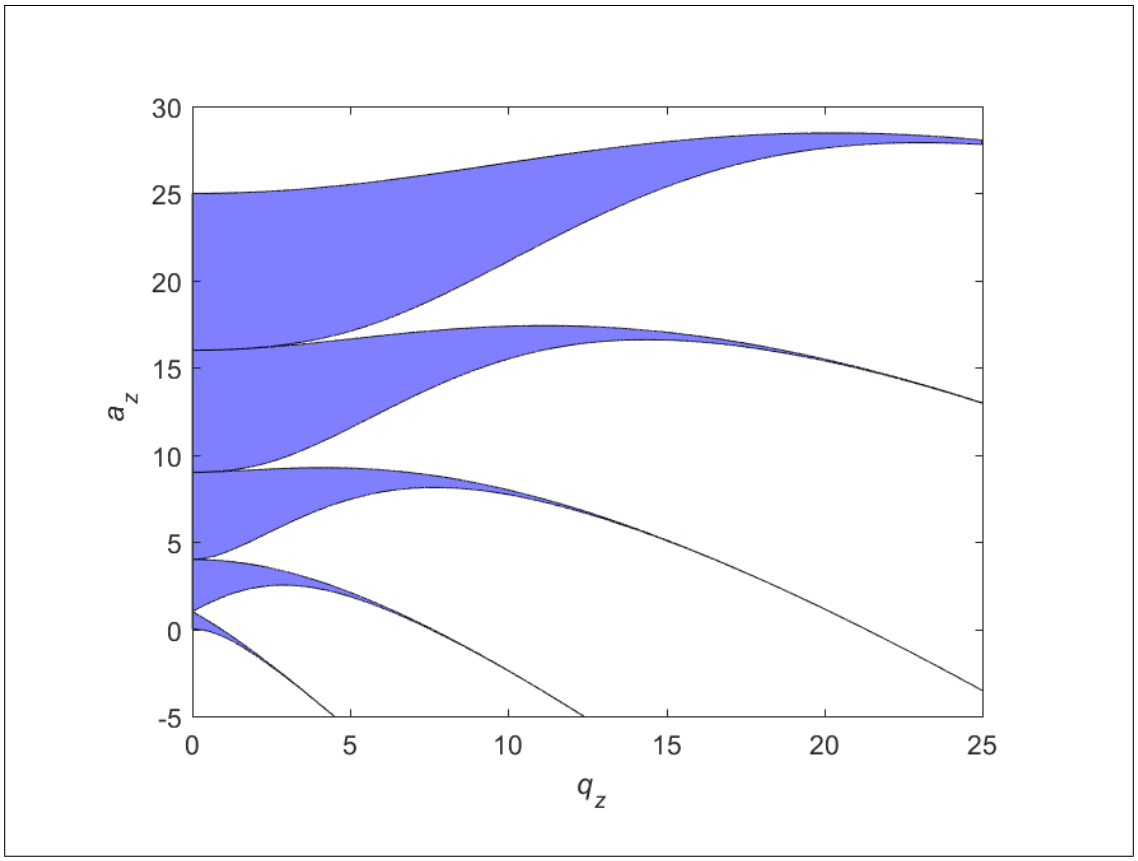

Figure 1.3: Stable regions of the Mathieu equation

Particles will only only stay trapped if the solutions for both the axial and the radial motion stay bound. Using the relations $a_z = -2a_r$ and $q_z = 2q_r$, the stability diagrams for both directions can be depicted in one plot, which allows to determine the parameters for stable trapping from the intersection of both regions. Figure 1.4 depicts stable regions for trapping. Note that for small values of a it is possible to trap positive and negative particles simultaneously.

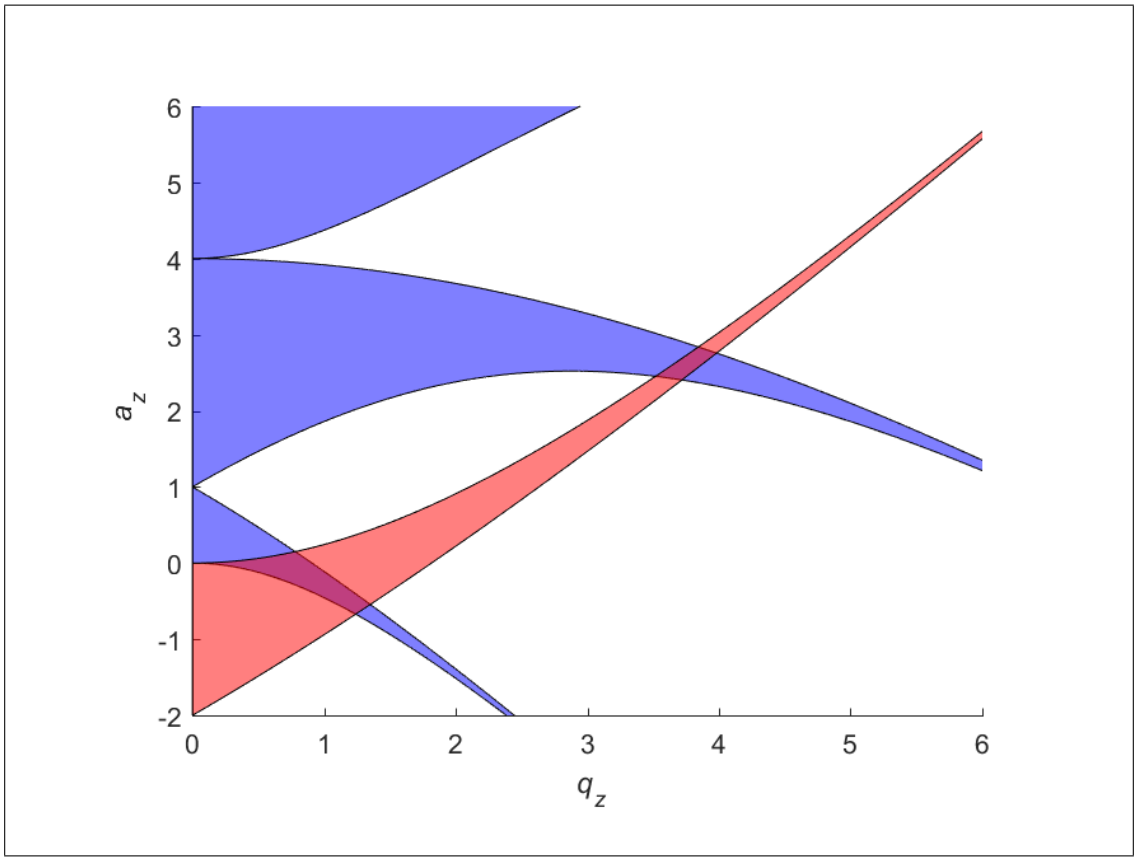

Figure 1.4: Blue: Stable trapping in axial direction. Red: Stable trapping in radial direction. Purple: The region for stable trapping lies in the intersection of the blue and red areas

In the case that the parameters a and q are chosen such that $a \ll q \ll 1$ it is possible to average the contributions of the AC voltage and receive an effective potential. This approach, called adiabatic approximation, is valid if the micromotion driven by the radio frequency is so small that the amplitude of the electric field stays almost constant over one oscillation. In this case, the stability parameter β can be estimated as

$$\beta^2 \approx a + \frac{q^2}{2} \tag{1.24}$$

and the solution of the ion motion governed by the Mathieu equation is approximated by

$$u(t) = R\left(1 - \frac{q}{2}\cos(\Omega t)\right)\cos(\omega t). \tag{1.25}$$

The parameter R depends on the initial conditions, Ω is the frequency of the micromotion given by the applied radio frequency, and $\omega = \frac{\beta}{2}\Omega$ is the frequency of the macromotion. As a,q and β are small, the macromotion is slow compared to the micromotion but has a larger amplitude. Figure 1.5 shows the simulated particle trajectories for different parameters a and q.

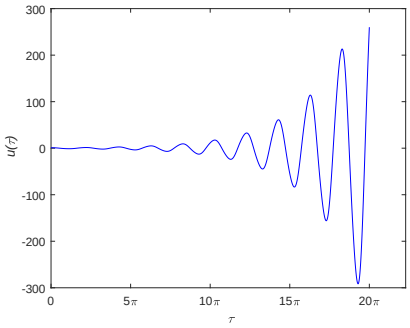

(a) $a = 1$, $q = 0.2$: The solution diverges

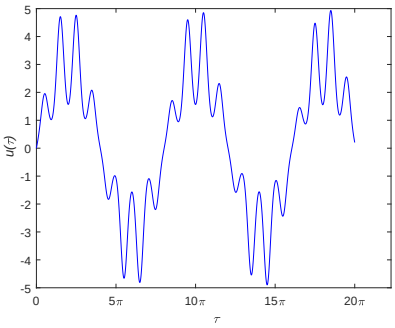

(b) $a = -0.6$, $q = 1.2$: The solution is bound

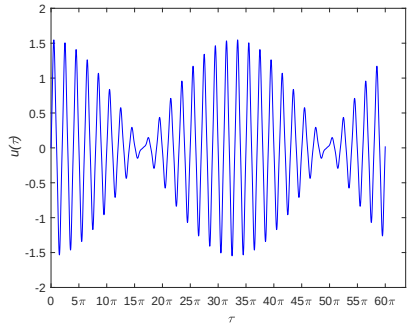

(c) $a = 0$, $q = 0.907$: The amplitude of the micromotion is large compared to the macromotion

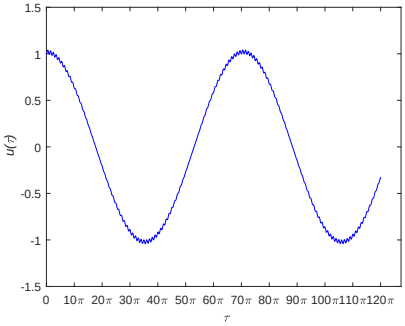

(d) $a = 0$, $q = 0.04$: If the adiabatic approximation is valid, the micromotion is small compared to macromotion.

Figure 1.5: Numerical solutions of the Mathieu equation for different values of a and q

1.3 Doppler Laser cooling

The possibility of cooling particles by irradiating them with light was first proposed independently by Hänsch and Schawlow [23] and Wineland and Dehmelt [24]. In 1978 Wineland, Drullinger and Walls [25] delivered the first experimental proof of laser cooling by reducing the temperature of Mg^+ ions trapped in a Penning trap to less than 40 K. The underlying idea adopted with laser cooling relies on the fact that an object's macroscopic temperature corresponds to the composing particles' velocity distribution on a microscopic level. In a hot cloud of atoms, the particles move faster than in a cold one. This relationship can be used to cool an ensemble of atoms by reducing the average velocity of its particles.

An atom's scattering rate γ for light depends on the light's frequency. Atoms will only absorb light with certain frequencies determined by the atoms' internal electronic configuration and their coupling to the light field. The scattering rate γ of an atom at rest with a transition at a

resonance frequency ω_R can be described by a Cauchy distribution [26]

$$\gamma(\omega) = \frac{\Gamma}{2} \frac{\frac{I}{I_{Sat}}}{4\frac{(\omega-\omega_R)^2}{\Gamma^2} + (1 + \frac{I}{I_{Sat}})}, \tag{1.26}$$

where I is the laser intensity, I_{Sat} the transition-specific saturation intensity and Γ is the resonant transition's natural linewidth.
The frequency perceived by an atom interacting with a beam of light depends on the atom's velocity relative to the beam of light. This effect, called Doppler effect, is analogous to the everyday life experience of a shift in sound frequency when driving past an ambulance that has its siren turned on. Particles moving towards the source experience a higher frequency in their rest frame than particles moving away. Given a source of light with frequency ω_0 in the laboratory frame, particles moving with velocity v towards the beam perceive a frequency ω' given by

$$\omega' = \omega_0 \sqrt{\frac{1 + \frac{v}{c}}{1 - \frac{v}{c}}} \overset{v \ll c}{\approx} \omega_0 (1 + \frac{v}{c}). \tag{1.27}$$

Combining the equations for the scattering rate and the Doppler shift in the limit of particles moving at non-relativistic speed ($v \ll c$) leads to the velocity-dependent scattering rate

$$\gamma(v) = \frac{\Gamma}{2} \frac{\frac{I}{I_{Sat}}}{4\frac{(\omega'(v)-\omega_R)^2}{\Gamma^2} + (1 + \frac{I}{I_{Sat}})} = \frac{\Gamma}{2} \frac{\frac{I}{I_{Sat}}}{4\frac{(\omega_0 \frac{v}{c} - \Delta\omega)^2}{\Gamma^2} + (1 + \frac{I}{I_{Sat}})} \tag{1.28}$$

with the detuning $\Delta\omega = \omega_0 - \omega_R$. The fact that an atom's absorption cross-section depends on its velocity by the Doppler effect makes it possible to address only atoms of a certain velocity v by detuning the light's frequency ω_0 such that it matches $\Delta\omega$ and the scattering cross-section becomes maximal.

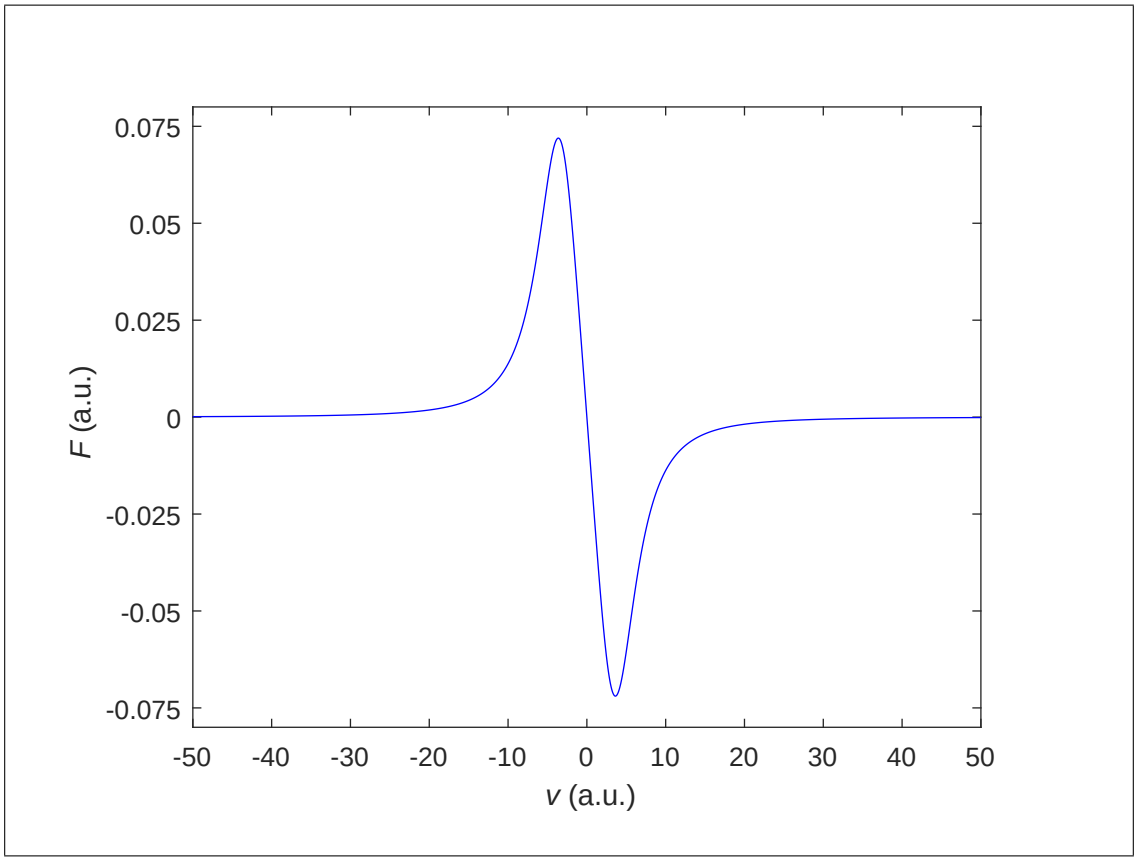

Figure 1.6: Radiative pressure force created by two counter-propagating, red-detuned laser beams acting on a particle as a function of its velocity. Note that the force always has the opposite sign of the velocity, thus slowing the particles down.

To cool atoms along one direction using this technique, two counter-propagating laser beams are superimposed with the atom cloud. Atoms moving towards one of the beams with a velocity matching the detuning of the light can absorb a photon and its momentum $\vec{p} = \hbar\vec{k}$. Given the scattering rate γ of the exited state, this can be interpreted as a force F acting on the particle.

$$F = \Delta p\gamma = \frac{\hbar k\Gamma}{2}\left[\frac{\frac{I}{I_{Sat}}}{4\frac{(\omega_0\frac{v}{c}-\Delta\omega)^2}{\Gamma^2}+(1+2\frac{I}{I_{Sat}})} - \frac{\frac{I}{I_{Sat}}}{4\frac{(\omega_0\frac{-v}{c}-\Delta\omega)^2}{\Gamma^2}+(1+2\frac{I}{I_{Sat}})}\right] \tag{1.29}$$

Note the additional factor 2 in the denominator, which is a way to account for power broadening from both beams [27]. In Figure 1.6 the force acting on an atom is depicted schematically. Particles moving towards the beam ($v > 0$) experience a negative force and vice versa, thus acting against the direction of motion and slowing the particles down.

When the atom emits a photon and returns to the ground state, it once again gains momentum equal to $\vec{p} = \hbar\vec{k}$. However, since spontaneous emission is isotropic, these momenta average out over multiple cooling cycles. Figure 1.7 depicts the different steps an atom goes through during

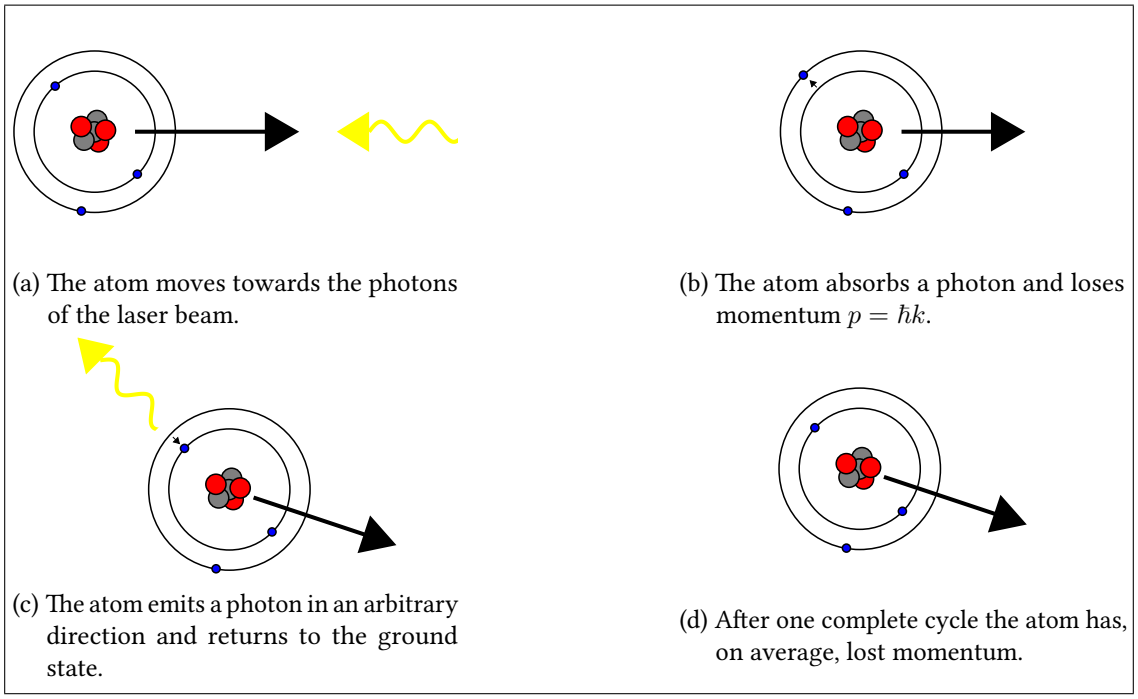

(a) The atom moves towards the photons of the laser beam.

(b) The atom absorbs a photon and loses momentum $p = \hbar k$.

(c) The atom emits a photon in an arbitrary direction and returns to the ground state.

(d) After one complete cycle the atom has, on average, lost momentum.

Figure 1.7: Principle of the Doppler cooling scheme

one cooling cycle.

By repeating multiple absorption and emission cycles, the atoms will slow down until the detuning of the laser no longer matches the atoms' velocity. To shift the atom back into resonance and continue the cooling process, the frequency ω_0 of the laser has to be changed or the transition's frequency ω_R modified. A tunable chirp laser [28] allows to modify the light frequency, while the transition frequency can be varied by using a Zeeman slower. This setup introduces a position-dependent magnetic field, which actively shifts the atoms' internal energy levels [29]. Regardless which of the methods mentioned above is used, the minimum temperature achievable by Doppler cooling is given by the Doppler temperature T_D [30]

$$T_D = \frac{\hbar\Gamma}{2k_B}. \tag{1.30}$$

Typical Doppler temperatures are on the order of 100 µK - 1 mK. As the trapped particles cool down, their associated Doppler width decreases. At small detunings, the probability of an atom which moves away from the laser absorbing a photon increases, thus reducing the cooling rate [31, p. 361]. At the same time, the atoms are heated by spontaneous emission. At the Doppler temperature the heating rate is equal to the cooling rate, and the temperature stays constant.

The cooling scheme described above assumes that the atom is a perfect two-level system and no other transitions than the resonant transition driven by the laser are present. In reality this does not have to be the case, which means that the excited atom can decay to different

states of lower energy. Depending on the level structure, electrons in these states might not interact with the laser beam. If these 'dark' states have sufficiently high life times, they have to be repumped for the cooling to continue.

More recently, new developments have allowed to overcome the Doppler limit [32], [33] Despite these advances in cooling of positive and neutral particles, laser cooling of negative ions so far has never been demonstrated. Negative ions are usually weakly bound systems and only few atoms exhibit two bound excited states with opposite parity. The low binding energy, also called electron affinity, causes the transitions to be low in energy, which means that a large number of absorption and emission cycles is necessary to reach cold temperatures. As a consequence, efficient cooling is only possible if the lifetime of the exited state is short. It is therefore necessary to use a dipole-allowed transition, causing the relaxation process to take place rapidly.

2 Experimental setup

2.1 Ion source

The source used to create negative ions is a Middleton-type ion sputter source (MISS). This type of ion source, developed by Middleton in 1982 [34], allows the creation of a large variety of molecular and atomic negative ions.
While there has been constant improvement on the original design, the main components of a MISS stayed the same: A sputter target, an ionizer and a reservoir containing Cs. Figure 2.1 shows a photograph of the opened ion source.

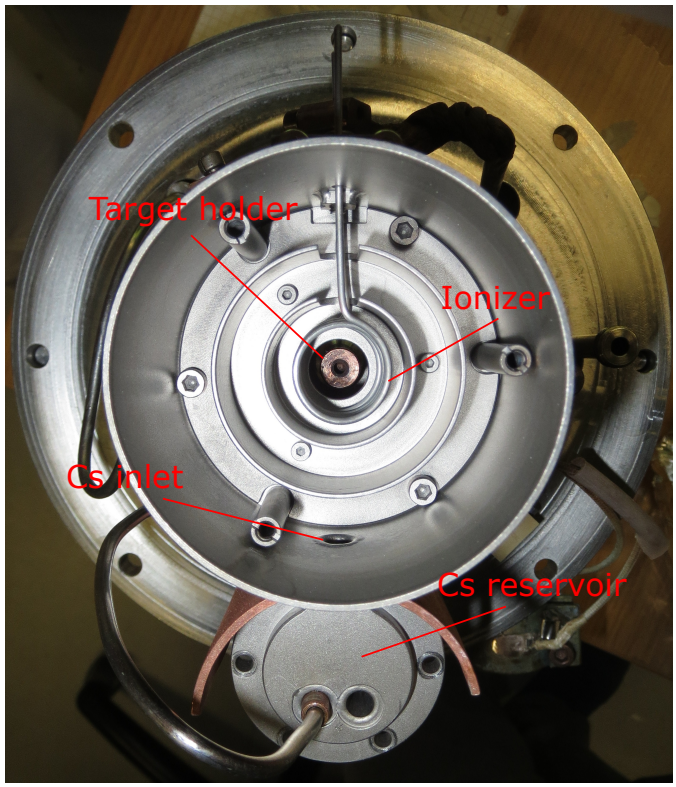

Figure 2.1: Photograph of the opened ion sputter source used to produce negative ions.

To produce anions, the temperature of the Cs reservoir is increased which causes the Cs to evaporate. The ionizer is heated to $\approx 1000\,\mathrm{K}$ by an electric current. As the binding energy of the valence electron in Cs is about 3,9 eV, the first ionization energy of Cs is lower than the tungsten ionizer's work function of 4.55 eV, which means that a Cs atoms coming into contact with the hot surface of the ionizer are likely to lose an electron and become positively charged. The ionizer is made from tungsten as its high work function and melting point are high. Instead of tungsten,the ionizer can be made from platinum, however, platinum ionizers bend easier during cleaning. By setting the ionizer to a positive potential with respect to the target, the Cs^+ ions are accelerated towards the target. The ions impinging on the target material have enough energy to detach atoms from the surface. This process is called sputtering. As typical electron affinities are on the order of 1 eV 2 eV and thus are lower than typical work functions [35], it is unlikely that the detached atoms are negatively charged. To increase the creation rate of anions, it is necessary to have a layer of neutral Cs atoms covering the the target. Some of the atoms leaving the surface pick up an additional electron from this layer and thus acquire a negative charge. The same electric field that accelerates the Cs^+ ions towards the target repels the anions and creates a constant beam of negative ions leaving the source. Typical currents achievable with Middleton-type sources are on the order of 100 nA – 100 uA [36] and depend strongly on the sputter target material. Figure 2.2 depicts the steps leading to the production of negative ions.

The production of negative ions relies on the ionization of Cs vapor. As the ionizer is positively charged with respect to the target, anions created by sputtering will deposit on the surface of the ionizer and change its work function. Cs atoms arriving at the ionizer no longer see a W surface, but rather the layer of deposited target material. If the target material's work function is lower than the ionization energy of Cs, it is more likely that the ionizer will lose an electron than the Cs atom. In this case Cs ionization is inhibited and the sputtering stops. The process of deposition of target material on the ionizer inhibiting ion production is called poisoning and has to be counteracted by cleaning the ionizer's surface. As the work function of La is approximately 3.5 eV [35] it is necessary to clean the ionizer's surface with hydrochloric acid after multiple days of operation. To circumvent the interruptions associated with exchanging and cleaning the ionizer, the experiments in this thesis are conducted with gold which has a work function of 5.10 eV – 5.47 eV [35] and won't inhibit Cs ionization.

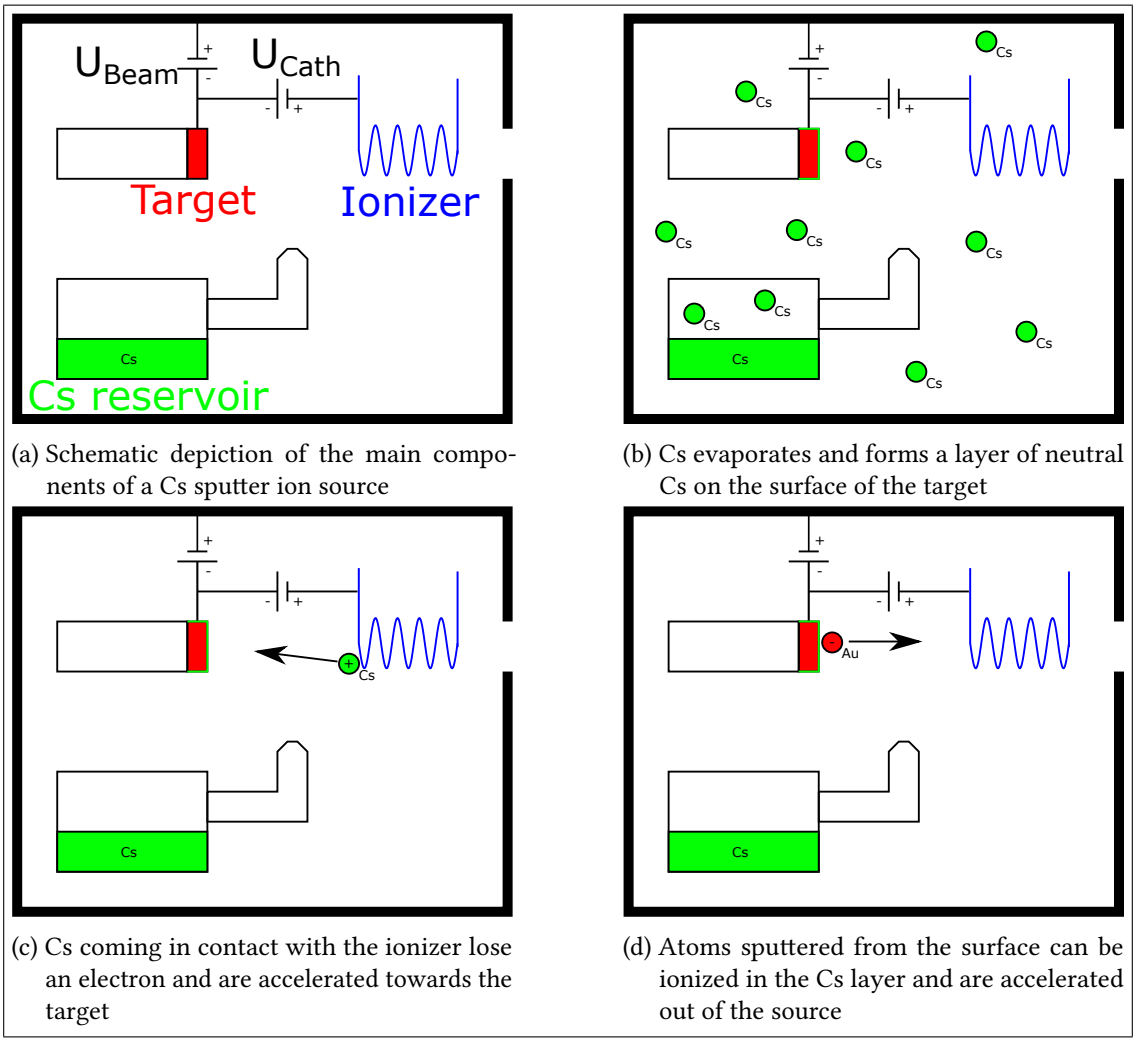

(a) Schematic depiction of the main components of a Cs sputter ion source

(b) Cs evaporates and forms a layer of neutral Cs on the surface of the target

(c) Cs coming in contact with the ionizer lose an electron and are accelerated towards the target

(d) Atoms sputtered from the surface can be ionized in the Cs layer and are accelerated out of the source

Figure 2.2: Production of negative ions in a MISS

The created anions leave the source with a kinetic energy corresponding to the acceleration voltage U_{Beam}. Along the beamline multiple Faraday cups can be inserted to measure the ion current at different positions. The source does not only produce the desired ion but also molecular ions of similar mass like LaO^- or LaH^- in the case of lanthanum. As these ions have a similar charge-to-mass ratio, it is necessary to remove them from the beam. For this purpose an electric mass-separating magnet is part of the beamline. This magnet forces the ions on a circular path whose curvature is determined by the magnitude of the magnetic field and the ions charge to mass ration. By varying the current flowing through windings of the magnet, it is possible to allow all ions with a specific mass to pass while removing most of the other ions.

2.2 Penning Trap

The Penning trap used in the experiment is a cylindrical trap consisting of 12 electrodes. Figure 2.3 shows a photograph of the trap and the wiring. The whole trap tower is located in the bore of a superconducting magnet and connected to the cryogenic environment by copper rods. The mechanical support rests on a reducer flange that holds the connectors for the individual trap electrodes.

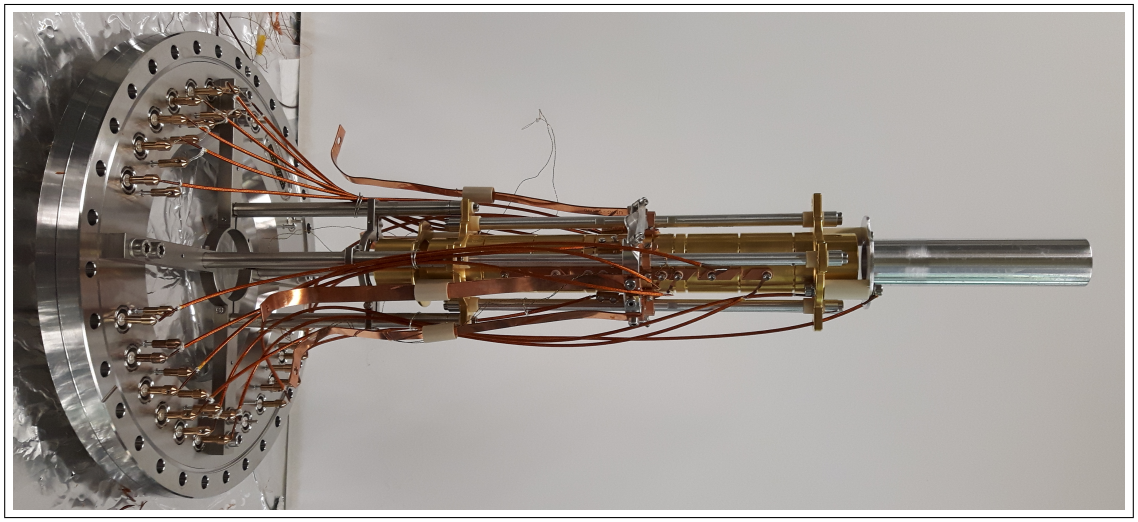

Figure 2.3: The Penning trap tower mounted on the new reducer flange

An electron gun which can be inserted into the beamline is located in front of the Penning trap. This electron gun allows the creation of a stream of electrons flying through the trap region. Thanks to their low mass, electrons stored in the Penning trap have a high cyclotron eigenfrequency. This rapid movement causes them to lose energy via synchrotron radiation, thus cooling down to lower temperatures than heavier ions trapped under the same conditions. Using the fact that particles of vastly different mass can be stored together in a Penning trap, this cold electron plasma can be used to precool heavier negative ions.

In the course of this thesis a new reducer flange was designed and installed allowing higher voltages to be applied to the trap. The old design had the advantage that every electrode is connected twice, which provides a way to verify that a voltage is applied to the electrodes. An additional advantage is the fact that the trap can be used even if one of the two wires breaks off the electrode. However, the maximum voltage that can be applied to the electrodes with this design was limited to $\approx 500\,\mathrm{V}$ as only the first two and last two electrodes were connected via SHV connectors. To trap ions at the high beam energies required for efficient transmission, it is necessary to be able to apply voltages up to multiple kV to the electrodes. The new design allows to put each electrode to a voltage up to 5 kV. To achieve this electric strength, all electrodes had to be connected via SHV connectors. Additionally, these connectors had to be spaced on the flange in a way that allows access to all connectors without interfering with the cross containing the moveable MCP and the Paul trap.

Apart from the flange modification, the wiring within the vacuum chamber had to be changed. To shield the Penning trap electrodes from picking up noise created by the radio-frequency drive of the Paul trap, high-voltage-proof vacuum-compatible cable was used to wire the Penning trap. The shielding was grounded on the reducer flange. The individual cables were bundled and attached to the rods supporting the electrode tower, thus preventing stress on the crimped connections on the flange and trap electrodes while at the same time keeping the cables in place.

2.3 Particle detection

To quantify the performance of the Paul trap, measurements of the amount of particles stored in the trap and the shape of the ion cloud were performed. While it is possible to measure the beam current directly, by connecting a femto-amperemeter to a Faraday cup that is inserted into the beamline, this type of measurement cannot be used to detect the amount of particles in the trap as the integration time of the analogue-to-digital converter used in the device is too large. Knowledge of the beam current allows a rough estimation of the number of particles impinging on the detector, which is used to calibrate the number of particles against the measured signal. To analyze the contents of the trap, the endcap in the back is opened, the ions are accelerated onto a micro-channel plate (MCP) detector and acquisition of the data is triggered at the same time. In the course of this thesis two different types of measurement were used. Time-of-flight measurements give information about the temporal distribution of particles hitting a detector, while imaging measurements allow statements about the shape and momentum distribution of the trapped particles.

Micro-channel plates allow the detection of charged and neutral particles as well as high-energy radiation. The following description of the working principle of an MCP assumes that particles are detected, however the same principles apply to the detection of radiation. An MCP consists of one or multiple plates in which slanted channels of about 10 µm diameter are embedded. A high voltage U_{Back} is applied between the front and the back of these plates with the back being on positive voltage with respect to the front. If a particle hits the front of a plate, it can detach some of the electrons from the surface of the plate. These electrons are accelerated through the channels towards the back and pick up enough energy to create more secondary electrons when they hit the wall of a channel. This results in a spatially contained avalanche of electrons. Typical ratios between the impinging charge and the charge exiting the plate on the back are on the order of 1×10^4 at a voltage difference of 1 kV. By mounting multiple plates back to back, this factor can be increased, however it should be noted that the total amplification is less that the product of the individual amplification ratios. The use of multiple plates has the additional advantage that the influence of residual gas ionized by the electron cascade on the signal is reduced. The number of electrons exiting the last plate is now large enough to be detected. A second potential U_{Screen} accelerates the electrons onto a phosphor screen. Upon impact, the electrons excite the P atoms locally. When the excited atoms return to the ground state, they release green light that can be imaged by a camera. Figure 2.4 depicts the detection

of an impinging AU^- ion schematically.

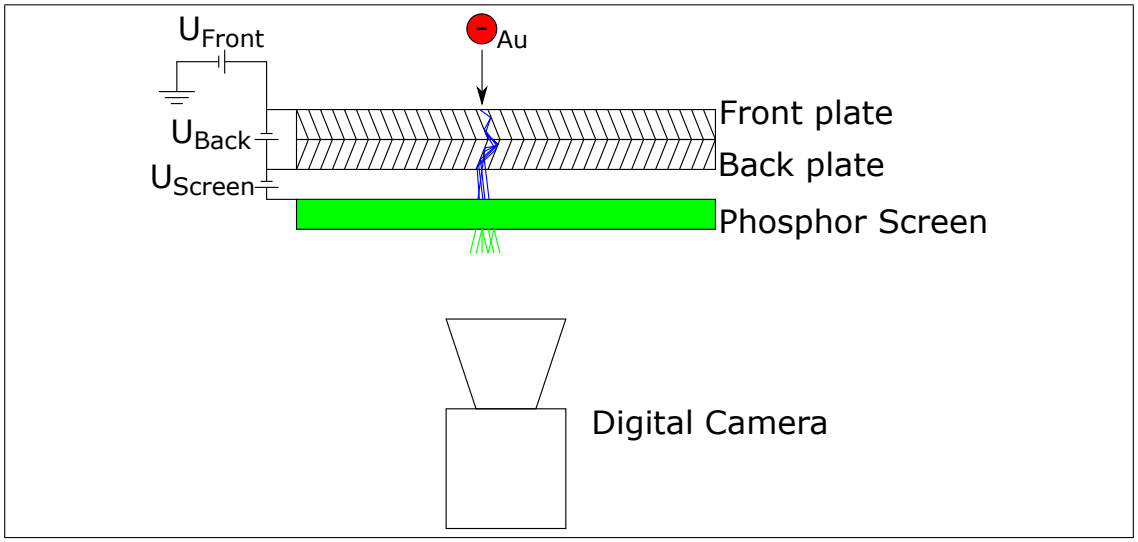

Figure 2.4: Schematic layout of a 2 layer MCP in chevron configuration with phosphor screen for particle imaging

In the original setup there were supposed to be two MCPs, one located directly behind the Penning trap and one located behind the Paul trap. The MCP behind the Penning trap is mounted on a pneumatic feedthrough and can be inserted into the beamline. This setup allows for detection of the contents of the Penning trap without blocking access to the Paul trap. This MCP is mounted on a high-duty pneumatic linear feedthrough, which allows movement even in the vicinity of a strong magnetic field. A mirror is located behind the phosphor screen of the MCP which allows optical access from outside. Figure 2.5 shows the mounting of the MCP.

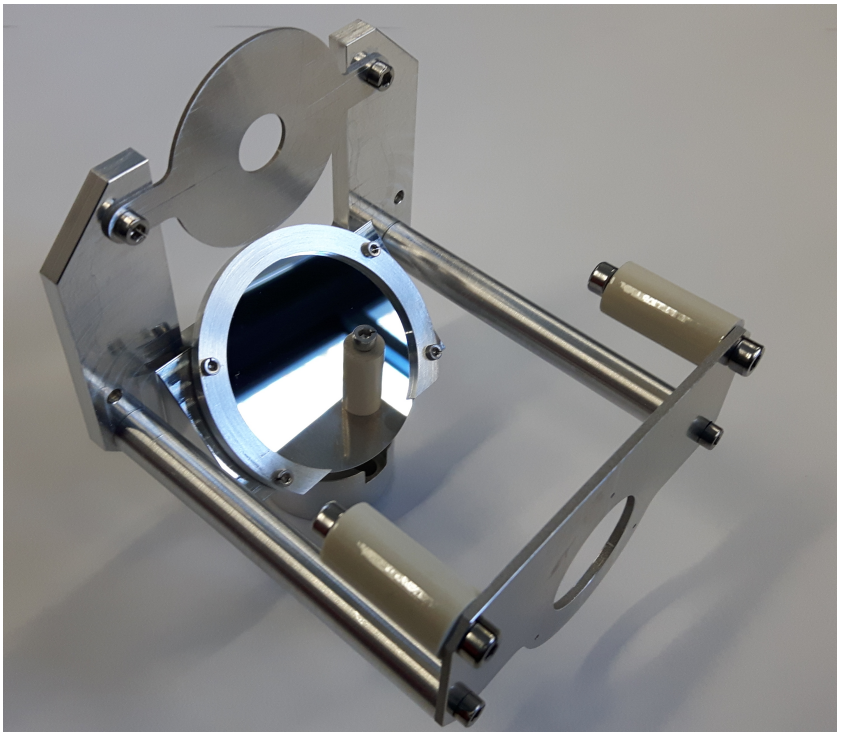

Figure 2.5: Mounting of the MCP behind the Penning trap

During the conditioning process, the MCP behind the Penning trap was damaged. Figure 2.6 shows the burned phosphor screen behind the MCP. We tried using the screen despite the visible damage but were unable to receive reasonable images.

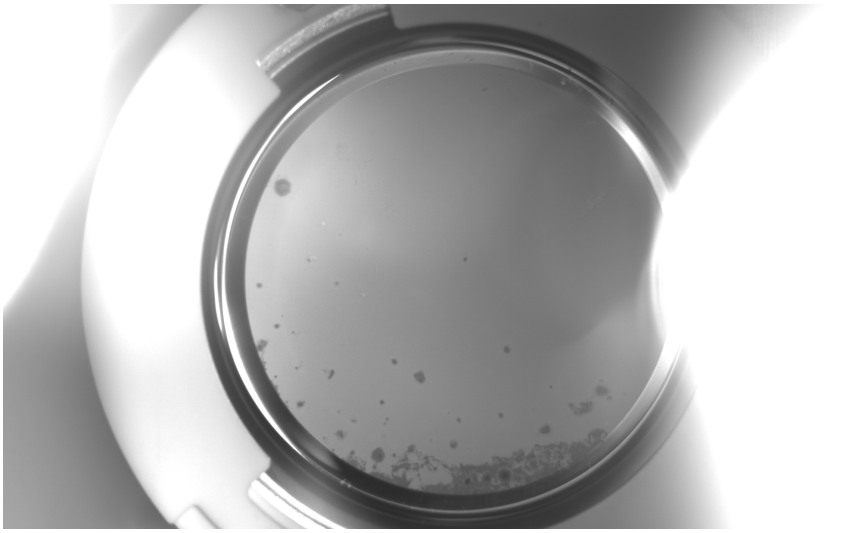

Figure 2.6: Photograph of the phosphor screen after conditioning

If the spatial distribution of the impinging ions is not of interest, the electrons exiting the back of the last MCP plate can be dumped onto a metal anode. Upon impact, the potential on this anode drops, as the electrons carry negative charge. This drop can be picked up by a triggered oscilloscope, thus giving information about the timing of the ion impact. In the course of this thesis the imaging MCP's phosphor screen was used for time-of-flight measurements instead of a metal anode. The circuit used for picking up the signal on the screen is depicted in figure 2.7.

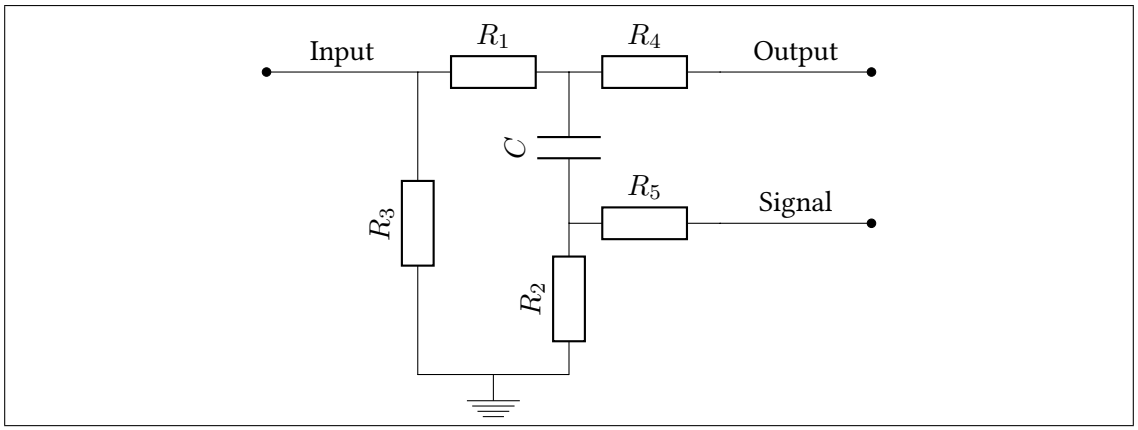

Figure 2.7: Circuit used for pick-up of the time-of-flight signal

When a particle hits the front face of the MCP, it creates an electron avalanche as described above. The electrons arriving exiting the last plate are pulled towards the anode or phosphor screen used for TOF pickup by a low voltage $U_{Screen} \approx 200\,\mathrm{V}$ without exciting the P. The electrons arriving on the screen cause the potential on the screen to drop. The resistor R_1 prevents large currents from flowing from the power supply towards the screen. Subsequently charges flow from the capacitor C to the phosphor screen which lead to a discharge of the capacitor. This discharge can be measured with an oscilloscope connected to the 'Signal' output of the circuit. The resistor R_2 determines the time constant for potential changes on C and thus can be used to trim the height and duration of the voltage drop. The values for $R_1 = 1.5\,\mathrm{M\Omega}$, $R_2 \approx 5\,\mathrm{k\Omega}$ and $C \approx 6\,\mathrm{nF}$ were determined empirically. An additional resistor $R_3 = 20\,\mathrm{M\Omega}$ was added between the input and ground to discharge the screen in case the power supply is disconnected during operation. R_4 and R_5 are $51\,\Omega$ resistors terminating the output connections.

2.4 Experiment control

In order to be able to change the potentials on the traps electrodes with precise timing, the whole experiment is controlled by a timer card (SpinCore PulseBlaster) that allows the creation of TTL pulses as short as 50 ns with a timing resolution of 10 ns. Tasks which do not need timing on such a level are controlled by a LabView VI. This method of experiment control allows to combine the precision timing of the PulseBlaster card with the high accessibility of experiment control via LabView. Figure 2.8 shows a schematic depiction of the two-layer control.

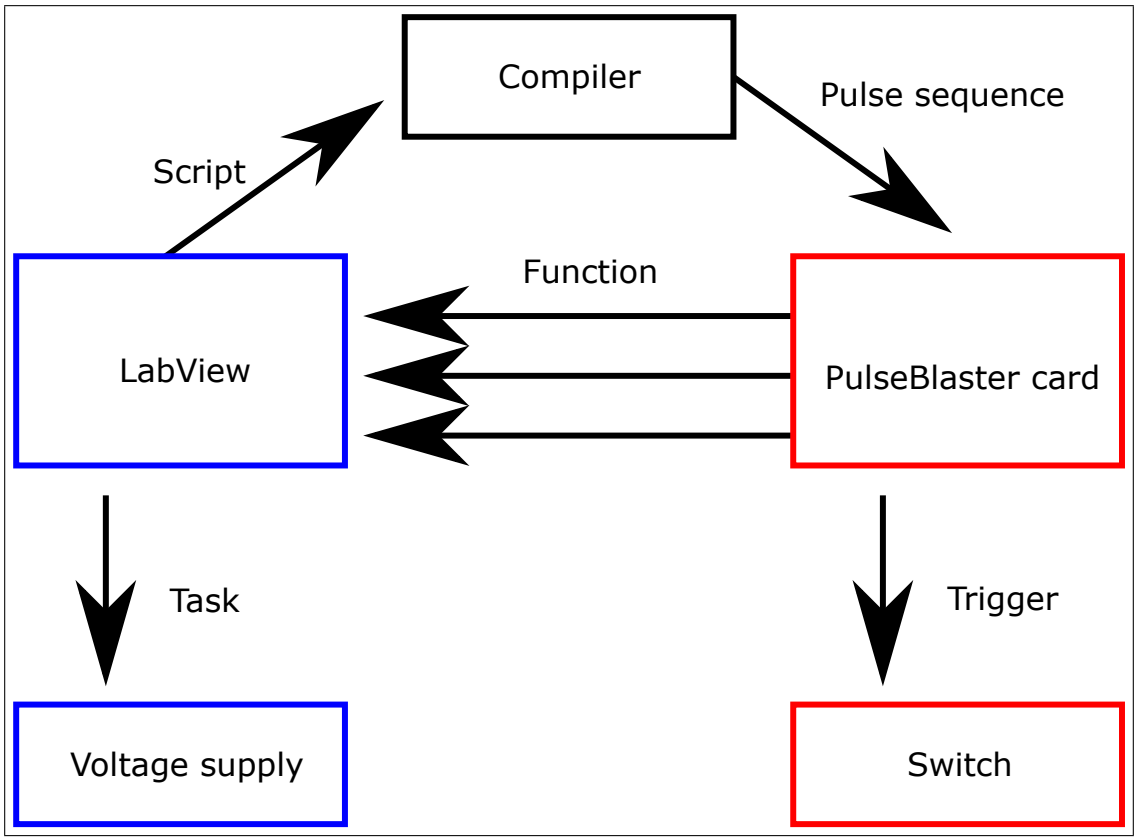

Figure 2.8: Two-layer control of the experiment. The red part depicts the high-precision-timing controlled parts of the experiment while the blue parts are controlled by LabView.

To conduct a measurement a LabView script is started. This script reads a file containing different tasks and their respective timing such as applying a voltage, triggering the oscilloscope or taking an image. A custom compiler written in this group transforms these tasks into a pulse sequence and sends it to the PulseBlaster card. The card runs this sequence and applies corresponding TTL voltages to its output channels. These channels are either directly used as a trigger for different parts of the experiment or connected to the computer running the LabView script. By reading out multiple channels via LabView it is possible to send a binary number to the computer. Different values of this number correspond to different tasks realised in LabView.

By sending multiple files to LabView it is possible to run a large number of measurements in sequence.

The advantage of this separation between programmatic flow controlled by the PulseBlaster card and execution of different tasks by LabView is that all timings are controlled by the low-jitter 100 MHz oscillator of the PulseBlaster card. Another advantage is that in case LabView crashes, the PulseBlaster card will finish the pulse sequence and deflect the ion beam by applying a voltage to the beam stop. This feature prevents possible damage to the experiment caused by continuously impinging ions.

2.5 Electronics

All power supplies used in the experimental setup are remotely controlled via LabView. Experience gathered while taking the Penning trap into operation showed that asymmetric changes of the voltage on the trap electrodes introduce noise and heat up the trapped particles. Trapping by reflecting the beam of charged particles on itself is only possible if the particles' kinetic energy in the trap region is close to the trap depth in axial direction. To pre-cool the ions with an electron plasma in the Penning trap it is therefore necessary to be able to lift the trap electrodes from $U_{Electron} \approx 100\,\mathrm{V}$ to $U_{Ion} \approx 1\,\mathrm{kV}$ without heating up the electrons. This lifting can be achieved by placing all voltage sources for the trap electrodes on a common reference potential. In this case the potentials applied to the trap electrodes with respect to ground are the sum of the reference potential U_{Bias} and the potentials supplied by the individual voltage supplies. In order to be able to float these voltage supplies to U_{Bias}, they have to be placed on a high-voltage platform which was realized in the course of a B.Sc. project [37].

In order to change the voltage on an electrode within a time short compared to the movement of the ions in the trap, multiple high-voltage switches are used. These switches have two high-voltage inputs and one high-voltage output. A TTL signal controls which of the input voltages is applied to the output. This setup allows to change the output voltage within nanoseconds, thus allowing control of the voltage applied to an electrode with precise timing no longer limited by the power supplies but rather the jitter of the control electronics. In order to be able to open and close the Paul trap in a short time, two new switches had to be installed. Figure 2.9 shows the wiring of these switches.

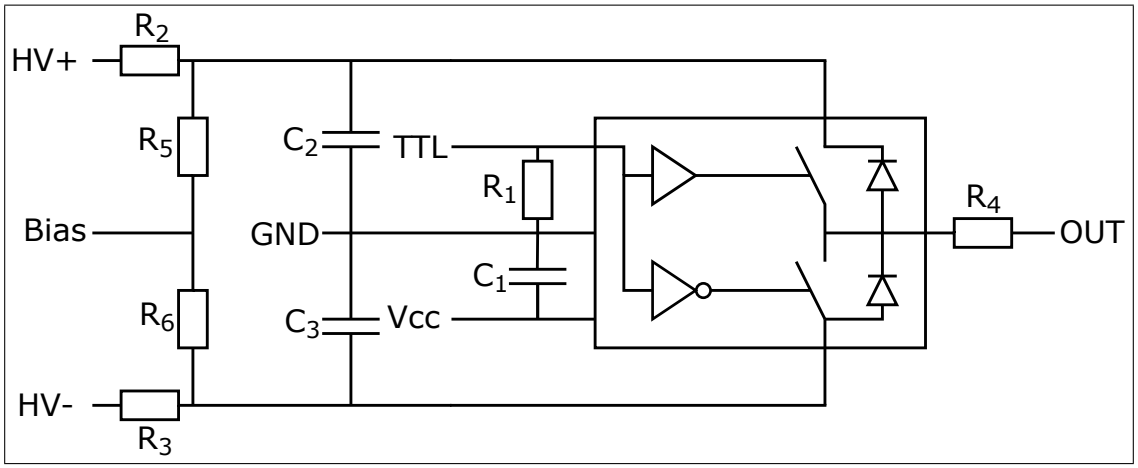

Figure 2.9: Circuit diagram of the two new switches

The new switches are located outside of the high-voltage cage, thus making it possible to connect their TTL inputs directly to the output of the PulseBlaster card. The TTL signal coming from the card is terminated by the resistor $R_1 = 51\,\Omega$. The supply voltage $V_{cc} = 5\,\mathrm{V}$ is buffered by the capacity $C_1 = 10\,\mu\mathrm{F}$. To trigger the switches located in the cage, an optocoupler has to be used to provide galvanic insulation between bias voltage and ground.
The high-voltage inputs HV+ and HV- of the switch are connected to the power-supplies via the resistors $R_2 = R_3 = 33\,\Omega$. These resistors protect the power supplies from voltages induced by the switching current. The voltages HV+ and HV- are buffered to ground with the capacitors $C_2 = C_3 = 24.7\,\mu\mathrm{F}$. The resistor R_4 on the output damps oscillations between the switch and the electrode. Additional discharge resistors $R_5 = R_6 = 20\,\mathrm{M}\Omega$ connected between the high-voltage inputs and bias were added to discharge the capacitors in case the external power supplies are disconnected while voltage is applied. We discovered that these resistors can't be connected between the high-voltage inputs and ground, as the power supplies providing the input voltages are located in the high-voltage cage. If the discharge resistors were connected to ground, a current would flow into the positive power supply causing it to malfunction.

3 Paul Trap

3.1 Initial design

The Paul trap used to store negative ions in our experiment does not have hyperbolic electrodes but rather consists of four cylindrical rods. Each rod is segmented into five separate electrodes which are isolated against each other. The first and last segments, seen from the direction of the incoming particles, have a length of 44.5 mm and 46.5 mm, respectively, while the three inner segments have a length of 14.8 mm. The rods have a diameter of 14.8 mm and are mounted parallel to each other in a square with a respective minimum distance $r_0 = 7$ mm between the rods and the trap center.

In a linear Paul trap, axial confinement is achieved by creating a common potential difference $U_{DC} = U_{Endcap} - U_{Center}$ between the outer rod segments and the three short segments in the center of the trap. If U_{DC} has the same sign as the ion's charge, the potential difference is confining in axial direction and repelling in radial direction. Note that it is therefore impossible to simultaneously store positive and negative ions in a linear Paul trap. The repelling part of the potential is counteracted by an alternating radio frequency field which is applied symmetrically to the rods. This voltage is supplied by a resonant circuit that creates a sinusoidal voltage $U(t) = U_{RF}\cos(2\pi ft)$ with a resonance frequency $f = 1.938$ MHz. The amplitude U_{RF} can be tuned up to approximately 750 V while the trap electrodes are connected. This voltage is applied to two opposite rods. The other two rods are connected to the same resonant circuit but the voltage is applied with a phase shift of 180°, effectively inverting the sign with respect to the other two rods. The differential amplitude U_{AC} of the voltage between two neighboring rods is therefore twice as large as the amplitude U_{RF} of the voltage applied to the individual rods. This configuration creates a time-dependent quadrupole potential near the trap center.

Assuming the rods are placed on the x- and y-axis, the equation of motion for an ion of mass m and charge Q in x- and y-direction are given by the equations

$$\frac{\mathrm{d}^2x}{\mathrm{d}\tau^2} + (a + 2q\cos(2\tau))x = 0 \tag{3.1}$$

$$\frac{\mathrm{d}^2y}{\mathrm{d}\tau^2} + (a - 2q\cos(2\tau))y = 0 \tag{3.2}$$

$$\text{with } a = \frac{4QU_{Geo}}{m\Omega^2 r_0^2},\ q = \frac{2QU_{AC}}{m\Omega^2 r_0^2} \text{ and } \tau = \frac{1}{2}\Omega t. \tag{3.3}$$

U_{Geo} is a voltage proportional to U_{DC} whose value depends on the trap geometry [38]. Using the knowledge gained in the discussion of the hyperbolic Paul trap, we see that the motion in x- and y-direction is governed by the Mathieu equation. As the parameter a is the same for the movement in both cases and the region of stability in a-q-space is symmetric with respect to the sign of q the parameter combinations that lead to stable trapping are the same for the motion in x- and y-direction. The requirement for axial confinement $QU_{DC} > 0$ restricts stable trapping to points with $a < 0$ as a describes the repulsive part of the potential created by U_{DC}. Figure 3.1 depicts the stability diagram for a linear Paul trap.

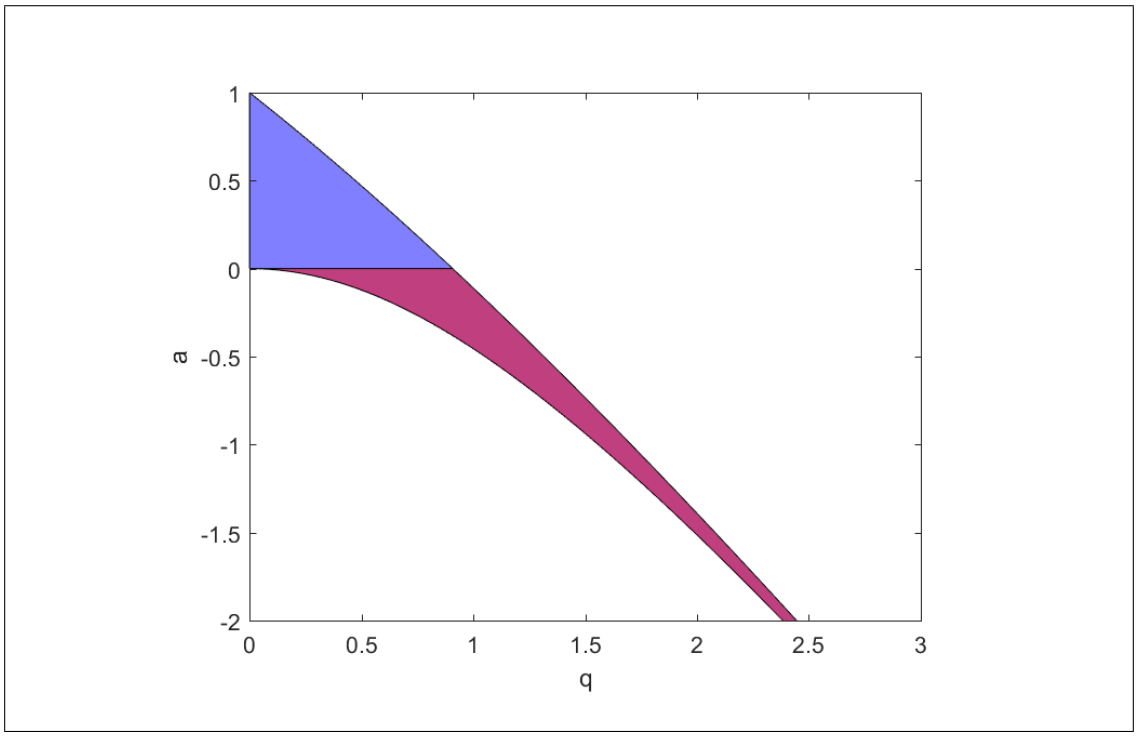

Figure 3.1: Blue: stable trapping in radial direction. Purple: stable trapping in all directions.

To compensate for the residual magnetic field created by the superconducting magnet of the Penning trap, a set of permanent magnets was placed around the trap. The field created by

these magnets cancels the intensity and gradient of the residual field in the trap center. In the initial design, the MCP detecting the particles in the Paul trap was mounted on an arm behind the base holding the trapping rods. Figure 3.2 shows the initial design of the Paul trap.

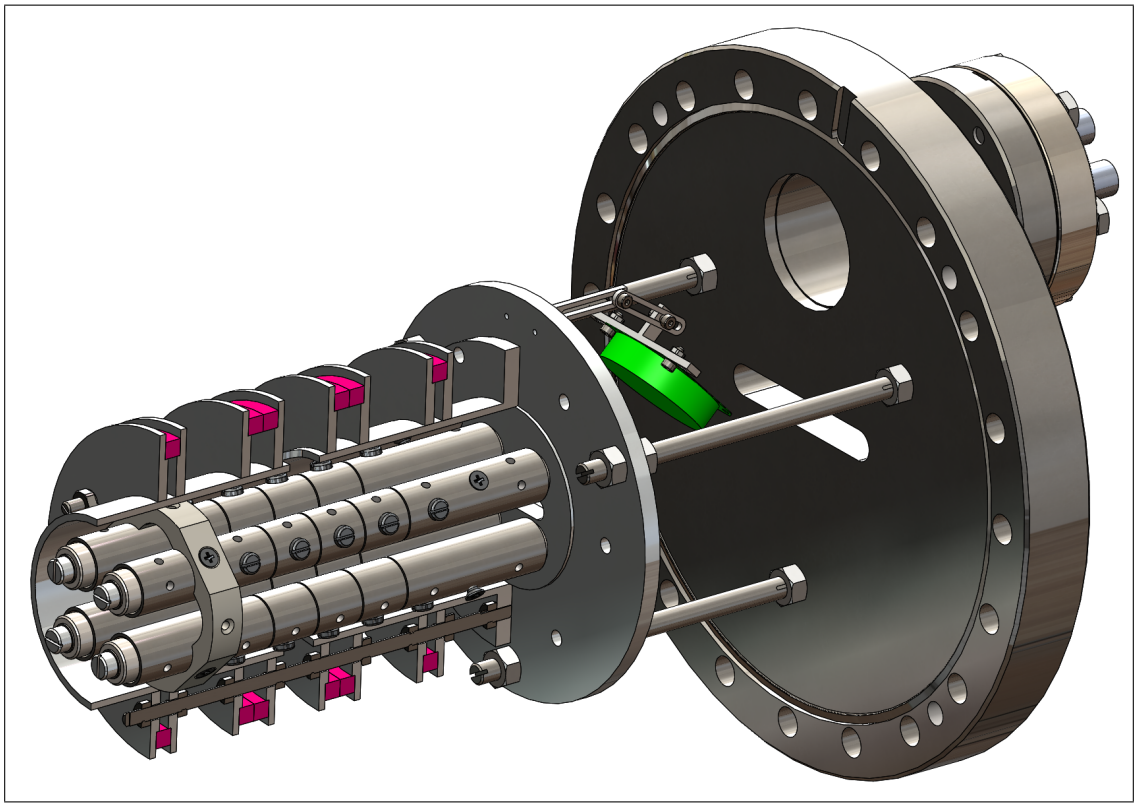

Figure 3.2: Sketch of the initial design of the Paul trap. The purple rings represent the compensation magnets. The green cylinder mounted on the metal arm shows the position of the MCP that can be tilted into the optical axis.

In the initial design, the Paul trap was mounted in two six-way CF160 crosses behind the Penning trap. An extension of the rods was supposed to help guiding the ions through the diverging magnetic field to the Paul trap. In this design the Paul trap was located far away from the magnetic field created by the superconducting magnet of the Penning trap. Figure 3.3 shows an overview over the initial design.

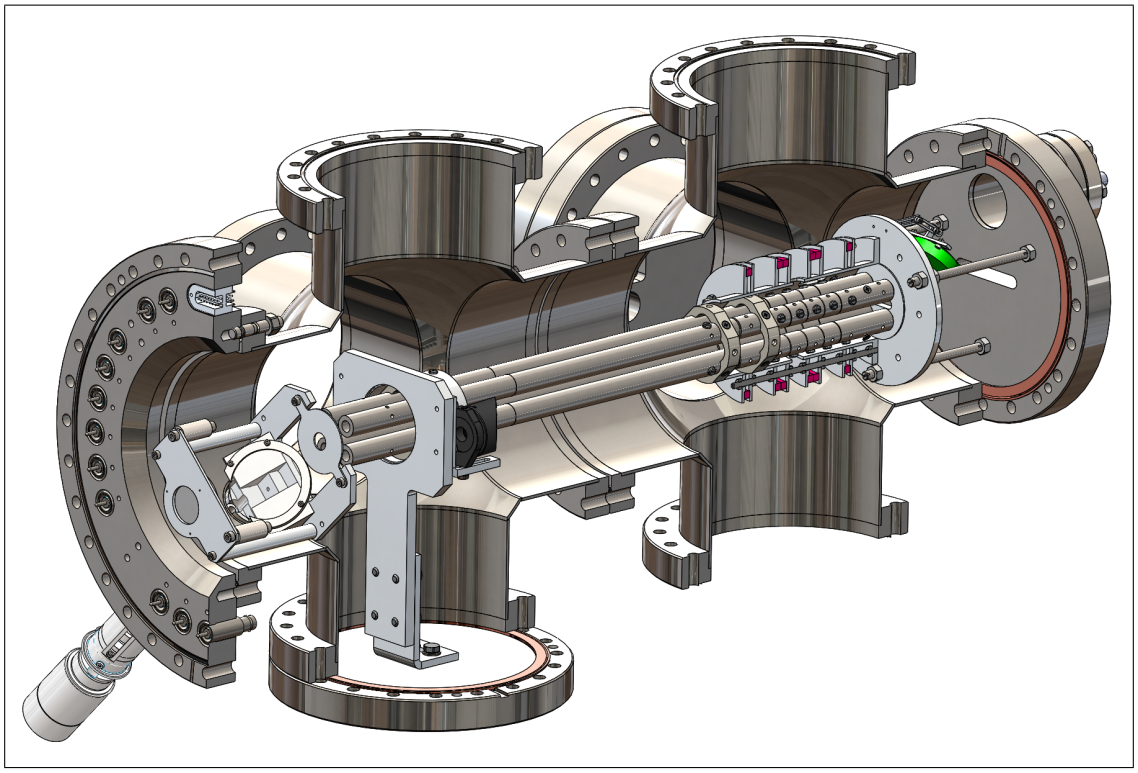

Figure 3.3: Sketch of the initial Paul trap section. Ions arrive from the left.

At the beginning of this work, the individual components of the Paul trap had already been manufactured but had never been assembled in the apparatus and tested.

3.2 Modification of the initial design

While wiring the Penning trap, it became clear that the mounting of the permanent magnets restricts access to the trap too much. It was decided to remove the permanent magnets and their housing and attempt direct trapping of the ion beam in the Paul trap without earlier capture in the Penning trap. This way the Paul trap can be operated while the superconducting magnet is off, thus removing the necessity to spatially separate the Paul trap from the Penning trap or compensate for the residual magnetic field. The new design therefore provides better access to the trap, both for electrical connection and optical interaction. Figure 3.4 shows an overview of the new Paul trap section.

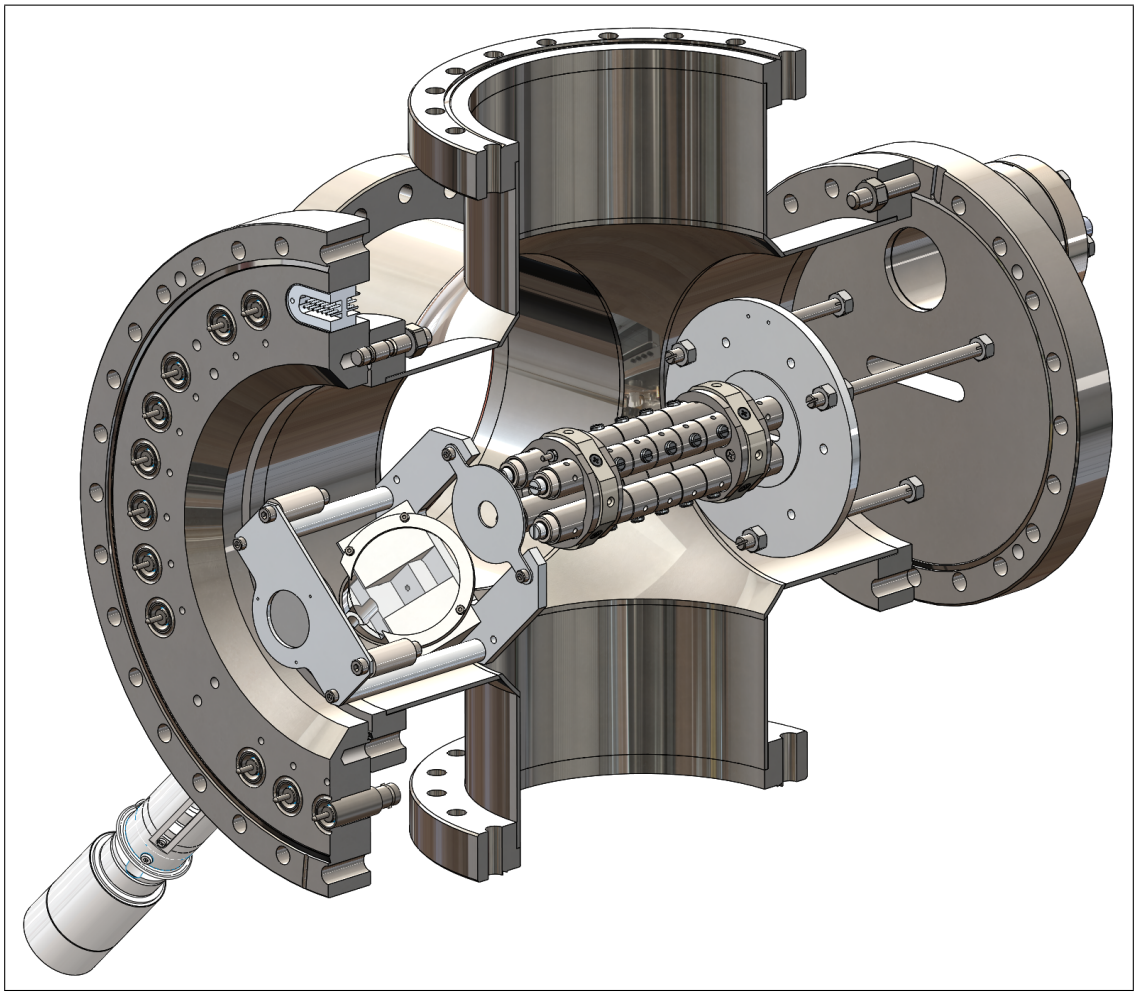

Figure 3.4: Sketch of the new design of the Paul trap section. The trap is mounted in a six-way CF160 cross located directly behind the Penning trap.

The circuit used to couple the radio frequency voltage to the rod electrodes made it impossible to switch the voltage applied to the last segments of the rods. Switching the voltage on an electrode within a short time requires large currents to flow as the electrode represents a capacity. To protect the power supplies creating the DC voltage applied to the rod segments from the radio frequency voltage, a resistor on the order of several MΩ is connected in front of the power supply as depicted in figure 3.5. This resistor limits the flowing current and makes fast switching of the voltage on the rod segments impossible.

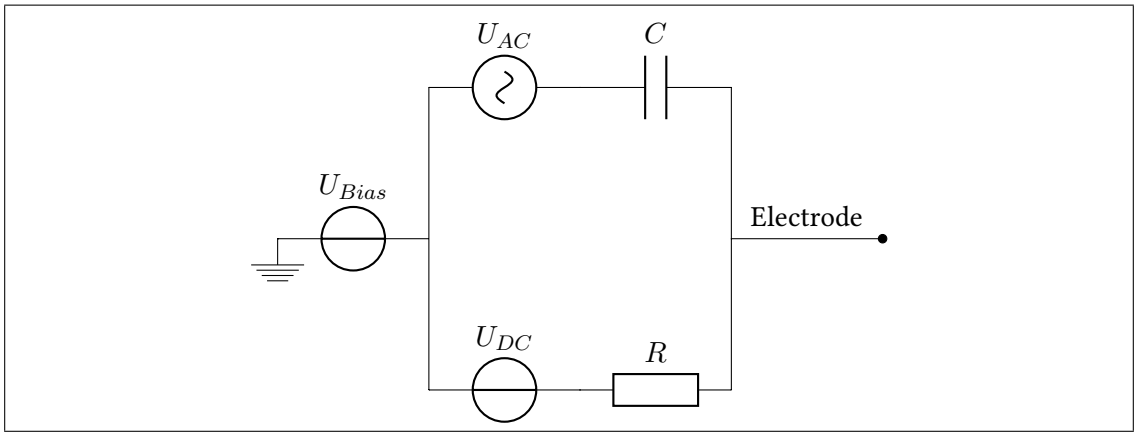

Figure 3.5: Simplified circuit diagram depicting the wiring of the Paul trap electrodes.

As switching of the end caps is essential for opening and closing the trap on timescales similar to the ion motion, two additional end cap electrodes were created. These electrodes have to protrude towards the center of the trap as otherwise the potential created by the end caps would be shielded by the rod electrodes. At the same time the electrodes must not block optical access in axial direction to keep open the option of laser cooling the axial motion. As a result, it was decided to mount the additional electrodes on the insulators which keep the rods in place. To be able to switch the potential of the end cap on both ends, a second insulator was mounted in the center of the last rod segment.

The new end cap electrodes consist of two pieces that are fitted to the shape of the insulators and are held together with two screws in axial direction. A simple shape for end cap electrodes providing axial particle confinement would be a cylinder containing four holes which allow the rod electrodes to pass through the end cap. While this shape provides confinement, it does not allow the ejection of the trapped ions in axial direction. In order to allow the particles to leave the trap if no voltage is applied to the end cap, the central part of the electrode is removed resulting in a cylinder with a hole resembling the shape of a four-leaf clover. Pedregosa et al. [39] discuss the efficiency of differently shaped end cap electrodes and suggest the aforementioned configuration. The final design of the electrodes realized in the course of this thesis resembles the general shape mentioned above but was adjusted to allow optical access in the x-z-plane. Two of the four bulks protruding towards the middle were removed while the other two were elongated to increase the electrodes' influence on the potential near the trap axis. Figure 3.6 shows a sketch of one of the electrodes.

Figure 3.6: Sketch of the additional electrodes added to enable switching of the end cap. The insulater providing the mechanical support for the electrode is depicted in green.

In the initial design opposite rod segments were supposed to be placed at the same DC voltage. To increase the options for control of the ion cloud's position in the x-y plane, it is of advantage to be able to control the voltage on each rod individually. As the circuit used to apply the voltages to the individual electrodes provides only 14 individually coupled channels, the total number of electrodes had to be reduced. It was decided to short-circuit the first, second and fifth electrode on each rod, respectively, which decreases the total number of independent rod segments from 20 to 12. During the assembly of the Paul trap, it was discovered that the ceramic disk holding the MCP has a radius similar to the spacing between the trap axis and the three threaded rods connecting the base plate of the Paul trap to the back flange. It was therefore decided to remove the arm holding the MCP and instead mount the detector by squeezing the ceramic plate between a combination of nuts and washers located on the threaded support rods. Figure 3.7 shows a photograph of the wired trap.

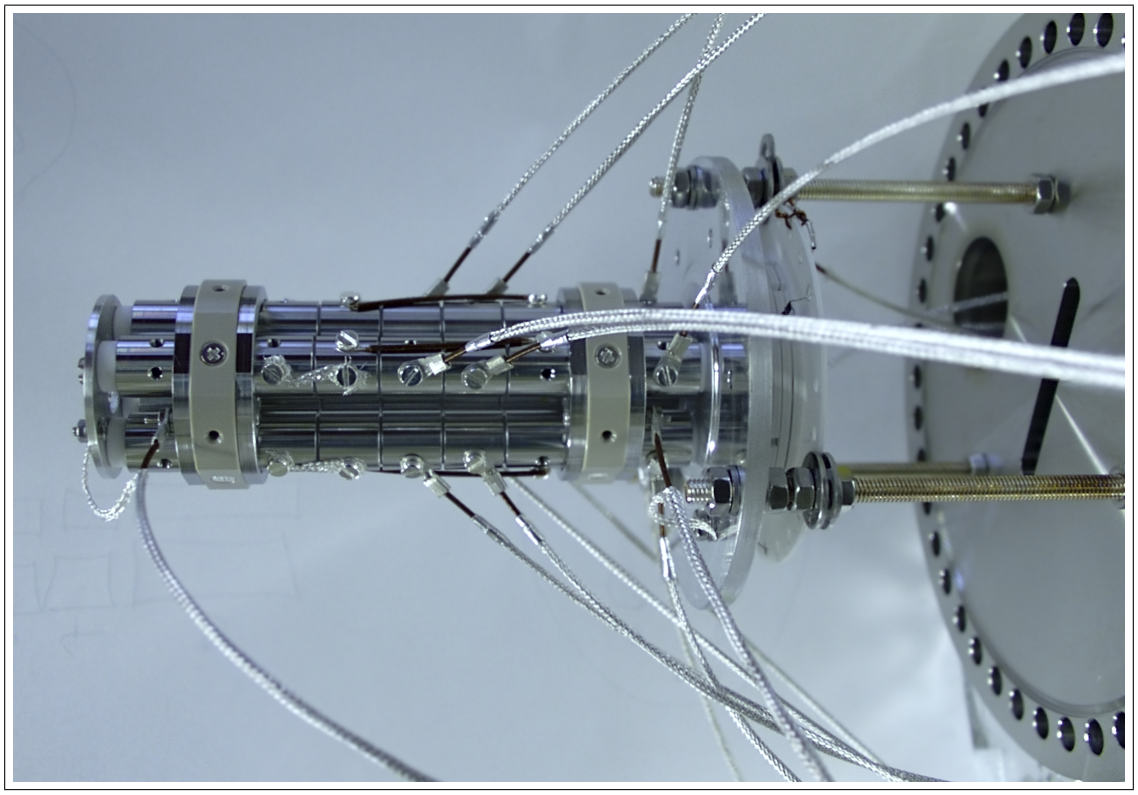

Figure 3.7: Photograph of the assembled Paul trap and the MCP mounted between the threaded rods holding the trap's base plate.

3.3 Simulations

The modifications described above alter the trapping potentials. To ensure that the switching electrodes create a potential strong enough to close the trap, the potentials as well as the motion of a trapped particle were simulated.

3.3.1 Calculation of the Paul Trap potentials

The potential $\Phi(x, y, z)$ created by the electrodes for given applied voltages U_{AC} and U_{DC} can be calculated by solving the Laplace equation in charge-free space $\nabla^2\Phi = 0$. To do this, the volume was divided into a Cartesian grid on which the Laplace equation is solved. The result is a three-dimensional array consisting of voxels at coordinates $x_\Phi = x_1, \ldots, x_n$, $y_\Phi = y_1, \ldots, y_m$ and $z_\Phi = z_1, \ldots, z_l$ with edge length $\Delta x_\Phi = \Delta y_\Phi = \Delta z_\Phi$. Figure 3.8 shows the model of the Paul trap used to calculate the potential.

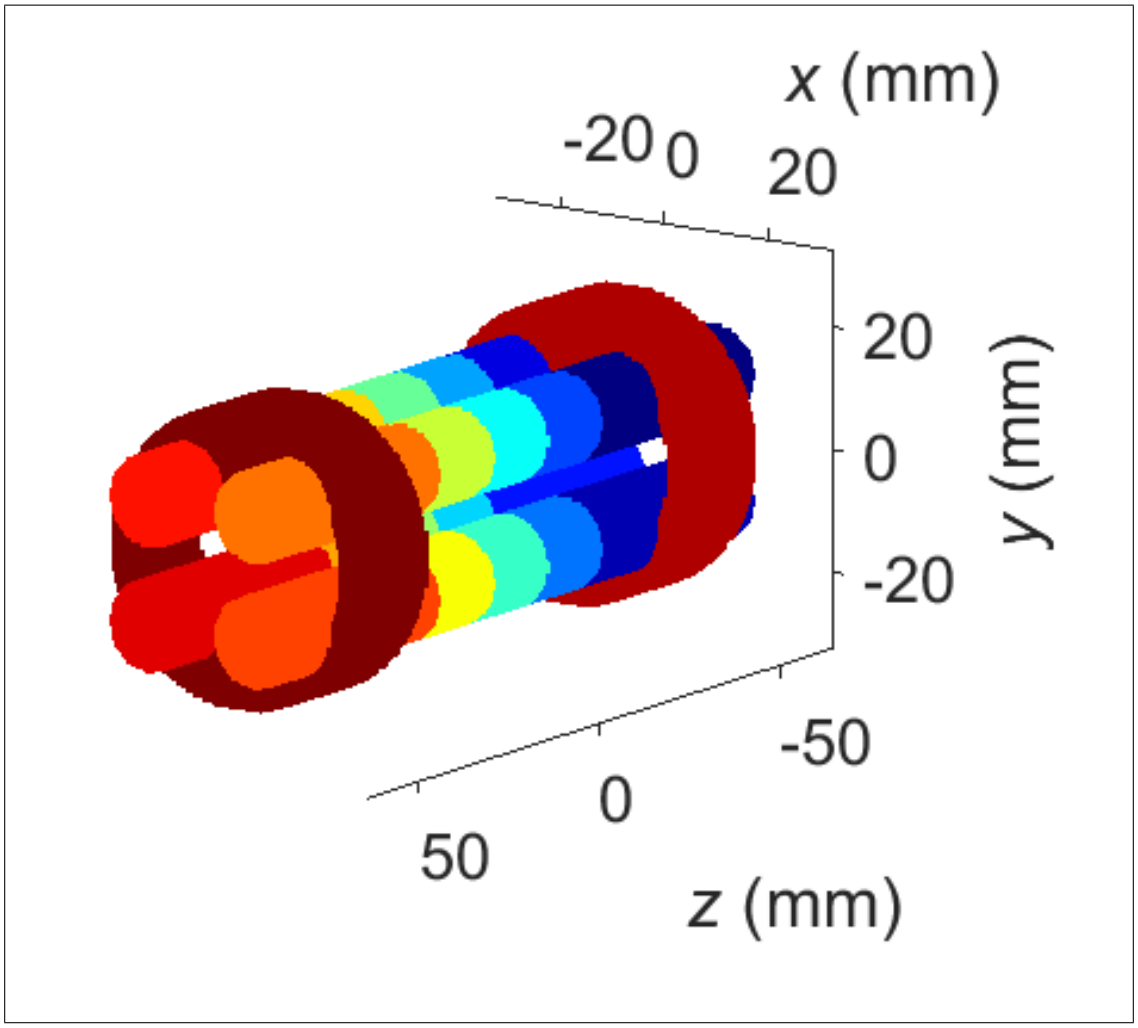

Figure 3.8: Discretized model of the Paul trap. The different colors represent the different electrodes.

Introducing the notation $\Phi(x_i, y_j, z_k) = \Phi_{i,j,k}$ the trapping potentials can be approximate by solving the discrete Laplace equation

$$\begin{aligned}(\nabla^2\Phi_{i,j,k}) \approx & \frac{\Phi_{i+1,j,k} + \Phi_{i-1,y,z} - 2\Phi_{i,y,z}}{\Delta x^2} \\ & + \frac{\Phi_{i,j+1,k} + \Phi_{i,j-1,k} - 2\Phi_{i,j,k}}{\Delta y^2} \\ & + \frac{\Phi_{i,j,k+1} + \Phi_{i,j,k-1} - 2\Phi_{i,j,k}}{\Delta z^2} \\ = & 0\end{aligned} \tag{3.4}$$

on this grid.

According to Eq. 3.4 $\nabla^2\Phi_{i,y,z}$ vanishes in a voxel if the potential $\Phi_{i,y,z}$ in this voxel is equal to the average of the potential in all neighboring voxels. This can be interpreted as a discrete formulation of Gauss' law. This fact can be exploited to find a numeric solution by repeatedly averaging the potential in each voxel over the potential in all neighboring voxels. This will cause the potential to diffuse into the charge-free space until the the Laplace equation is satisfied. Figure 3.9 shows the calculated potential created by one of the end cap electrodes after a different number of iterations.

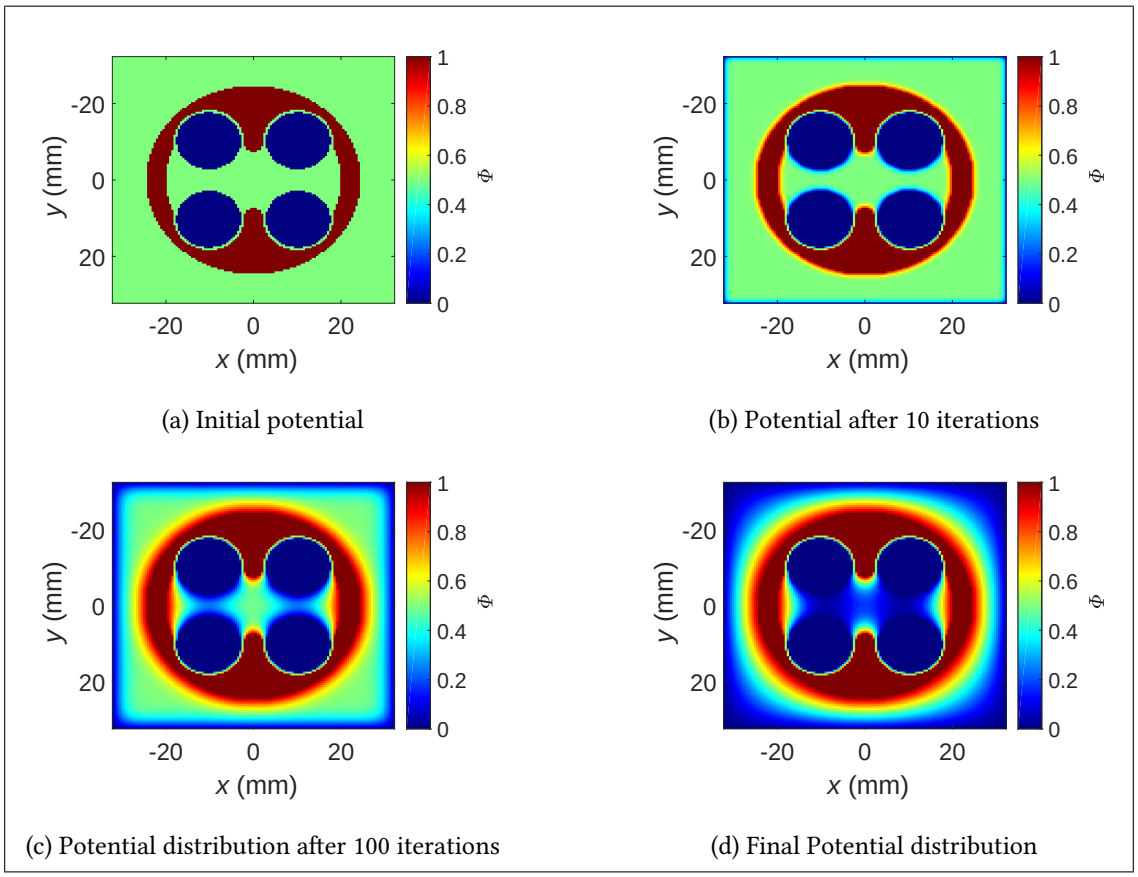

(a) Initial potential

(b) Potential after 10 iterations

(c) Potential distribution after 100 iterations

(d) Final Potential distribution

Figure 3.9: Calculated potential distribution for a different number of iterations.

The algorithm implementing this method can be described by the following steps:

1. Create a grid G containing a discrete model of the trap electrodes $E_1 \dots E_n$.
2. Select an electrode E_i and set the potential of the corresponding voxels to 1.
3. Set the potential of all other electrodes to 0.
4. Create two new grids G_{High} and G_{Low} with the same dimensions as G1. Initialise the potential in G_{High} as 1 and in G_{Low} as 0.
5. Set the potential of each voxel corresponding to an electrode to the value specified in G.
6. Average the potential of each voxel in G_{High} and G_{Low} over its neighbours.
7. Calculate the maximum difference between G_{High} and G_{Low}.
8. Repeat steps 5 - 7 until the maximum difference is lower than the desired threshold.
9. Save the average of G_{High} and G_{Low} for each voxel in a new grid G_i.
10. Repeat steps 2 - 9 for every electrode in G.

As the maximum potential is 1 and the minimum potential is 0, G_{High} and G_{Low} give upper and lower bounds for the potential in a voxel. Figure 3.10 shows how G_{High}, G_{Low} and their difference change for a voxel on the z-axis in the center of one of the end caps with an increasing number of iterations. Both curves converge to the same value. The final estimation of the potential is the mean between the values given in G_{High} and the values given in G_{Low}.

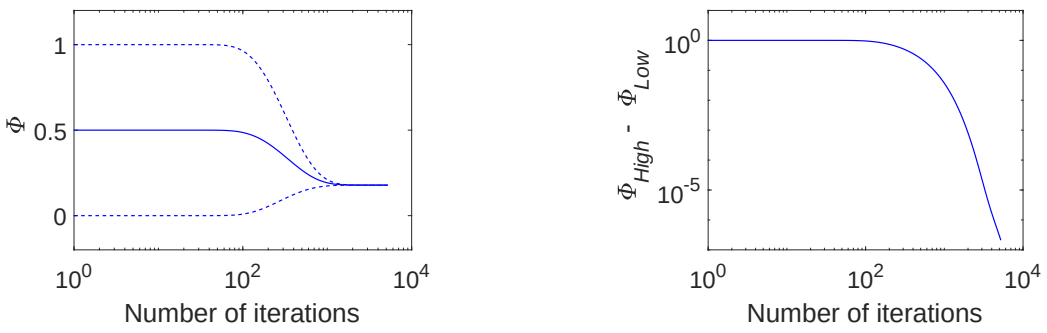

(a) Continuous line: Simulated potential. Dashed lines: Upper and lower bounds.

(b) Difference between upper and lower bounds.

Figure 3.10: Evolution of the simulated potential and its upper and lower bounds with increasing number of iterations.

As the Laplace equation is linear we can determine the overall potential G_{tot} for arbitrary voltages $U_1 \dots U_i$ on the electrodes $E_1 \dots E_n$ by adding the scaled individual solutions G_i:

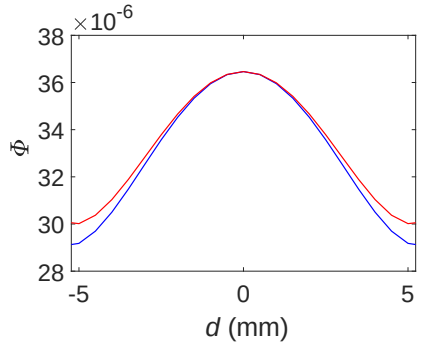

(a) Blue: Potential in x-direction, Red: Potential in y-direction

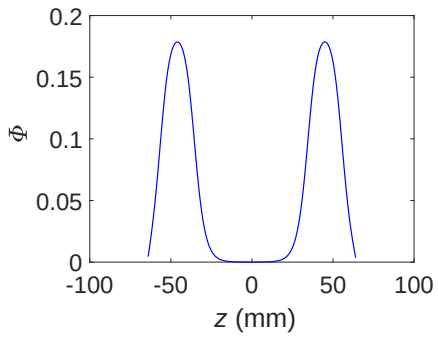

(b) Relative potential in z-direction

Figure 3.11: Potentials along the x-, y- and z-directions in through the trap center

$$G_{tot} = \sum_{i=1}^{n} U_i G_i \tag{3.5}$$

Having calculated the potentials created by all electrodes, we can investigate the potential in the trap center. Figure 3.11 shows the relative potentials created by the end cap electrodes as a function of the distance d from the trap center in x-, y- and z-direction. Note that the potential in y-direction drops slower than the potential in x-direction. This asymmetry is caused by the fact that the end cap electrodes protrude to the trap center in the y-direction.

These simulations suggest that the potential closing the trap on the z-axis is about 17.85 % of the potential applied to the electrode, which means that trap depths of up to 100 eV in axial direction can be achieved if the mean voltage difference between the end caps and the rods is provided by a 650 V voltage supply.

3.3.2 Simulation of particle movement

The solution of the potential $\Phi(x, y, z)$ on the grid allows us to estimate each component of the electric field $\vec{E}(x, y, z) = -\nabla\Phi$ as the finite difference between two neighboring voxels

$$\vec{E}(x + \frac{\Delta x}{2}, y + \frac{\Delta y}{2}, z + \frac{\Delta z}{2}) = - \begin{pmatrix} \frac{\Phi(x+\Delta x,y,z)-\Phi(x,y,z)}{\Delta x} \\ \frac{\Phi(x,y+\Delta y,z)-\Phi(x,y,z)}{\Delta y} \\ \frac{\Phi(x,y,z+\Delta z)-\Phi(x,y,z)}{\Delta z} \end{pmatrix}, \tag{3.6}$$

thus creating a second array of voxels at positions $x_E = x_1 + \frac{\Delta x}{2} \dots x_{n-1} + \frac{\Delta x}{2}$, $y_E = y_1 + \frac{\Delta y}{2} \dots y_{m-1} + \frac{\Delta y}{2}$ and $z_E = z_1 + \frac{\Delta z}{2} \dots z_{l-1} + \frac{\Delta z}{2}$. We can now use this grid to estimate the electric field at an arbitrary point not corresponding to a point on the grid by linearly interpolating between the points on the grid. This allows us to numerically solve the equation of motion for a trapped particle with mass m and charge Q. To calculate the particle's trajectory, we transform the second-order differential equation for the particle's position $\vec{r}(t)$ into two first-order differential equations

$$\dot{\vec{r}}(t) = \vec{v}(t) \tag{3.7}$$

$$\dot{\vec{v}}(t) = \frac{Q}{m}\vec{E(t)}. \tag{3.8}$$

This set of differential equations is subsequently solved with the 'ode45' algorithm integrated in Matlab [40]. Figure 3.12 shows the simulated trajectory of an Au^- ion with mass $m = 197$ u for a frequency $f = 1.938$ MHz with a DC voltage $U_{DC} = -500$ V applied to the end caps and an AC voltage $U_{AC}(t) = \pm 450\,\text{V}\sin(2\pi f t)$ applied to the rods.

The simulations suggest, that the end cap electrodes successfully confine the particle to the trapping region. As expected, the motion in z direction is not harmonic as the potential created by the end caps vanishes quickly towards the trap's center. The radial motion seems to be dominated by the macromotion, which is expected as the value for $|q| = 0.1214$ given by Eq. 3.3 is small. Nevertheless, the small micromotion driven by the applied radio frequency is visible as a superimposed oscillation with period T close to 0.5 µs.

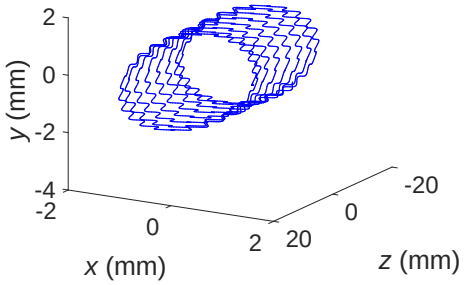

(a) Simulated particle trajectory for $t < 100\,\mu s$.

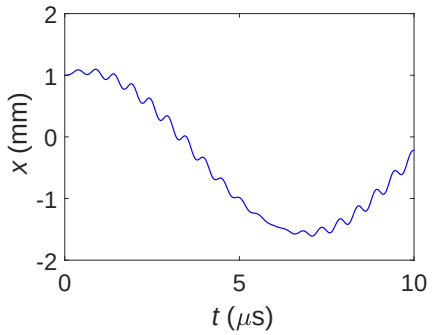

(b) x component as a function of time

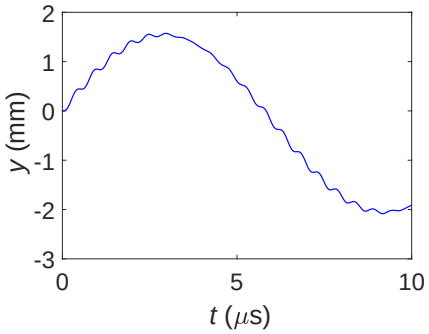

(c) y component as a function of time

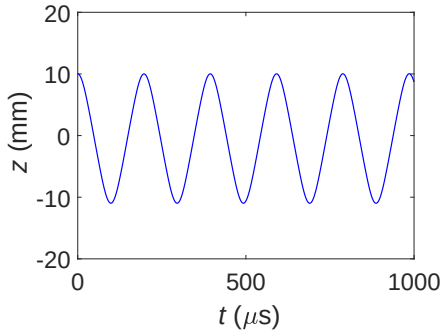

(d) z component as a function of time

Figure 3.12: Simulated motion of an Au^- ion initially resting at the point $x = 1\,\text{mm}$, $y = 0\,\text{mm}$, $z = 10\,\text{mm}$.

4 Experimental results

All measurements presented in this thesis were conducted with Au^- ions to prevent problems arising from source poisoning. While the mass of Au^- ions is about 1.4 times as large as the mass of La^- ions, the frequencies required for stable trapping are similar enough to justify working with gold. Unless otherwise stated, the Paul trap was operated at a frequency of $f = 1.938\,\text{MHz}$, a differential amplitude of $U_{AC} \approx 1200\,\text{V}$ and no DC voltage between the different rod segments. The q value for these parameters is $|q| = 0.16$, given by Eq. 3.3. To load the trap, all electrodes were floated to the bias voltage $U_{Bias} = -850\,\text{V}$ close to the acceleration voltage $U_{Beam} = -1006\,\text{V}$ of the ion source. Unless otherwise stated, voltages given for the trap electrodes are always measured with respect to bias. The end caps were put to $-45\,\text{V}$ on the end cap located on the side of the incoming beam and $-500\,\text{V}$ on the end cap close to the MCP. In this configuration, ions will enter the trapping region and be reflected by the end cap on the downstream end of the trap. Collisions between incoming and reflected ions can lead to a transfer from axial to radial momentum which causes the particles to lose enough energy in radial direction to become trapped. This technique has been used successfully in earlier experiments with the Penning trap.

To calibrate the measured luminosity against the number of particles arriving on the MCP, the beam current was measured with a femto-amperemeter. By gating the voltage on the beam stop, a rough estimation of the number of particles arriving on the MCP was determined. The luminosity was measured for different voltages on the back plate, which allowed for a calibration of the number of particles. To account for differences in signal caused by different energies of the ions impinging on the MCP, the Paul trap was loaded, the bias voltage was changed and the ions were released onto the MCP. As the conditions for the loading were identical in all cases, the number of trapped ions can be assumed to be identical as well which allows to calibrate for the influence of the dumping voltage.

It should be noted that the absolute number of particles given by this method is probably not accurate, as the beam current was measured on the front face of the MCP used for imaging. This leads to the problem of secondary electrons created by the impinging particles leaving the surface, thus changing the measured current. Even on a relative scale comparisons between particle numbers might be flawed by systematic effects, as the beam current is known to drift over time leading to a difference in loading conditions. The 1σ confidence bounds given in the following discussion of the experimental results are determined from the fits and do not account for these systematic shifts.

4.1 Comparison between simulated and measured potential

In order to quantify the performance of the additional end cap electrodes, we used the Paul trap as a beam guide. The rod electrodes as well as the first end cap were set to a bias voltage U_{Bias}, while the voltage on the second end cap was varied. By measuring the number of particles n arriving on the MCP, we compared the influence of an increase in bias voltage U_{Bias} to an increase in the voltage U_{Endcap} applied to the end cap. Figure 4.1 shows the MCP signal as a function of U_{Bias} and U_{Endcap}.

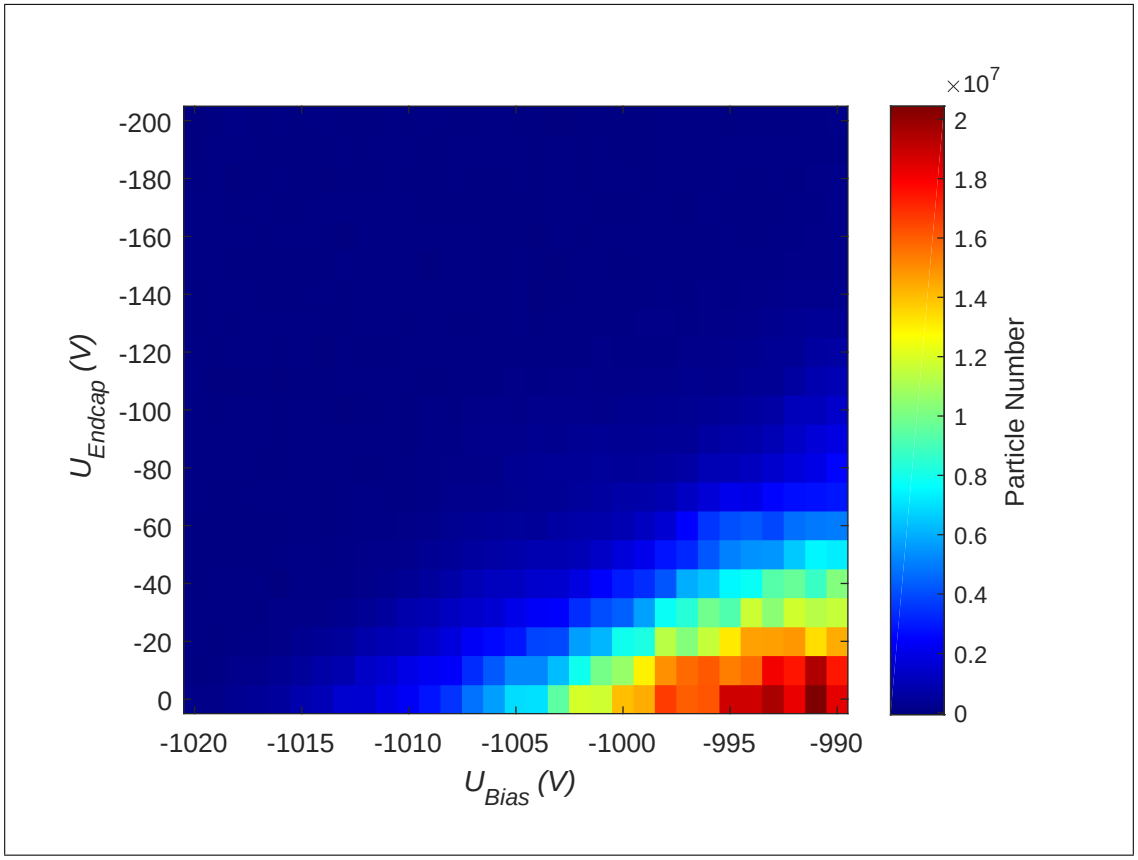

Figure 4.1: Density plot of the number of particles as a function of bias voltage U_{Bias} and voltage on the end cap U_{Endcap}

As the rods of the Paul trap are long compared to the spacing between the rods, we can assume that the potential in the center of the trap is equal to U_{Bias}. This allows us to determine the relationship between the stopping potential U_{Stop} and the number of ions. Figure 4.2 shows the number of particles N as a function of U_{Bias} at $U_{Endcap} = 0\,\mathrm{V}$. This relationship between N and U_{Bias} can be approximated by a power law $U_{Bias}(N) = U_0(N - N_0)^p$. The parameters that fit the data best were found to be $U_0 = -1033\,\mathrm{V}$, $N_0 = 71.4 \times 10^3$ and $p = 0.211$. Note that only data points with N between 1×10^5 and 1.3×10^7 were considered in the fit.

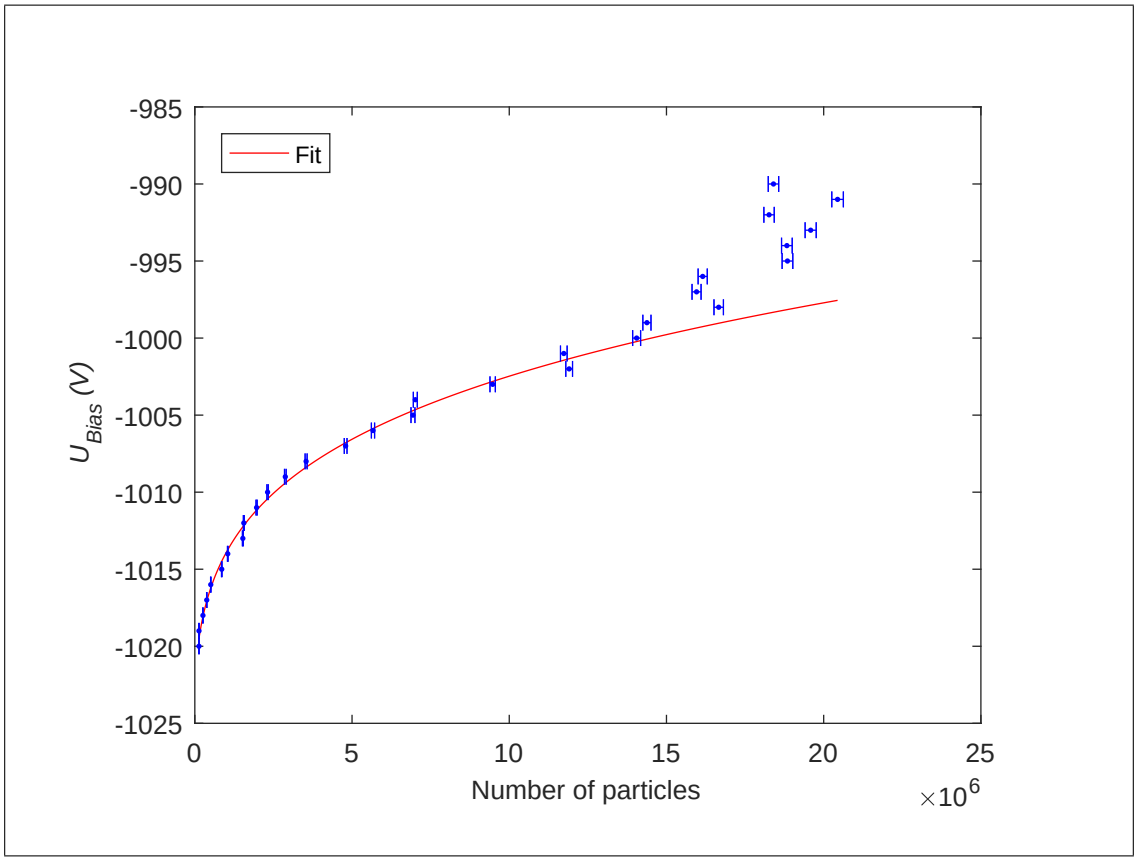

Figure 4.2: Bias voltage U_{Bias} as a function of the number of particles N for $U_{Endcap} = 0$. The red line represents the best fit of the function $U_{Bias}(N) = U_0(N - N_0)^p$.

We can now use this function to assign each pair of U_{Bias} and U_{Endcap} an equivalent stopping voltage U_{Stop} that allows the same number of ions to reach the MCP if it was applied as the bias voltage. This stopping voltage is equal to the sum of the potentials created by the bias voltage and the end cap on the trap axis. Figure 4.3 shows U_{Stop} as a function of U_{Bias} and U_{Endcap}.

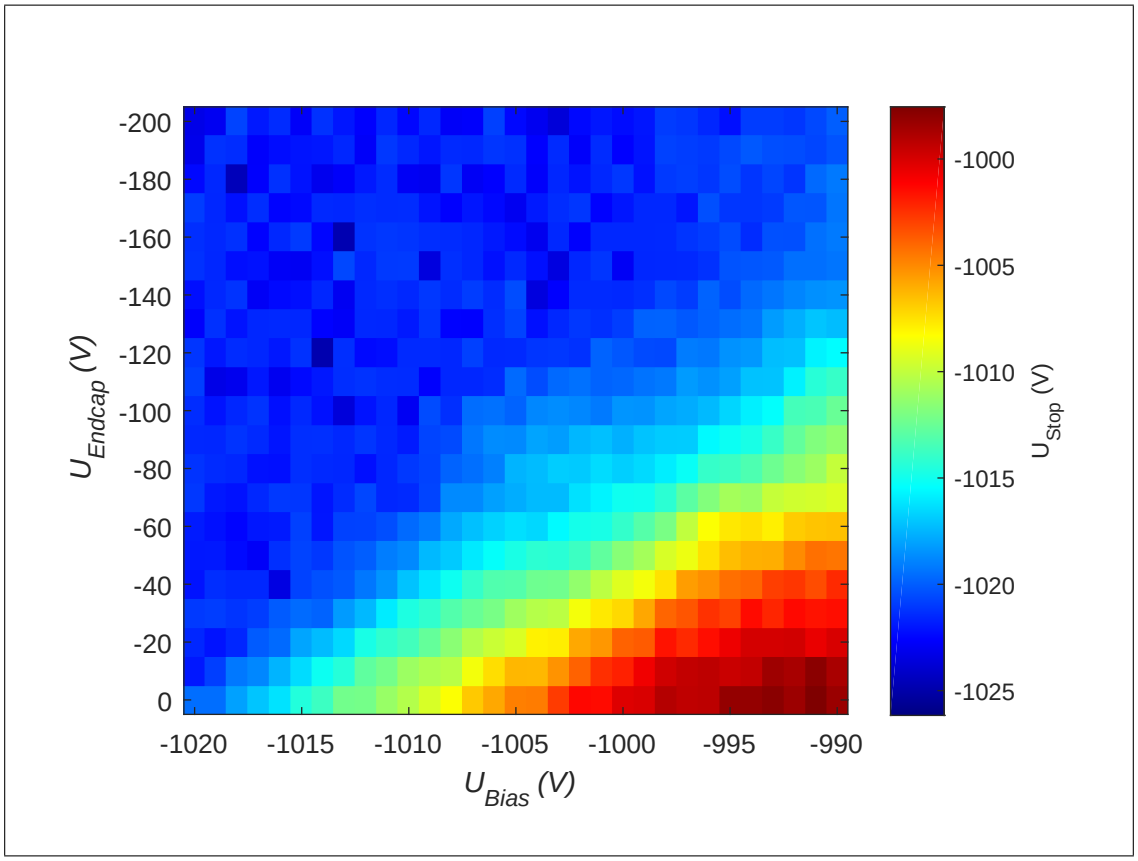

Figure 4.3: Equivalent stopping voltage U_{Stop} as a function U_{Bias} and U_{Endcap}. As expected U_{Stop} increases with U_{Bias} and U_{Endcap}.

If the particles are confined to the trap center by the radio frequency voltage the stopping potential can be described as a superposition of the potential created by the bias voltage and the additional potential created by the end cap:

$$U_{Stop} = a\, U_{Bias} + b\, U_{Endcap}. \tag{4.1}$$

The geometrical factors a and b can be determined by fitting Eq. 4.1 to the data shown in Figure 4.3. As the function used to assign the stopping potential is only valid for points with particle numbers between 1×10^5 and 1.3×10^7 all other points were ignored in the fitting process. The fit yields $a_{Exp} = 1.0011(2)$ and $b_{Exp} = 0.181(3)$ with the errors corresponding to the 1σ confidence intervals. While a deviates slightly from the value of $a_{Theo} = 1$ expected by theory, b_{Exp} agrees within 1σ with the value $b_{Sim} = 17.85\,\%$ gained from the simulation.

4.2 Loading time

The number of trapped particles depends on the duration during which the trap is loaded. The number of particles that can be trapped simultaneously depends on the trap depth and is

limited by their space charge. To determine an upper limit for the number of particles, the trap was loaded for different amounts of time, ranging from 10 s to 3 h. After loading, the particles were stored for 2 min allowing them to thermalize by evaporative cooling. The number of ions dumped on the MCP after 2 min of storing is shown in Figure 4.4. As the error bar are of similar size as the data marker, the error bars are not included the figure.

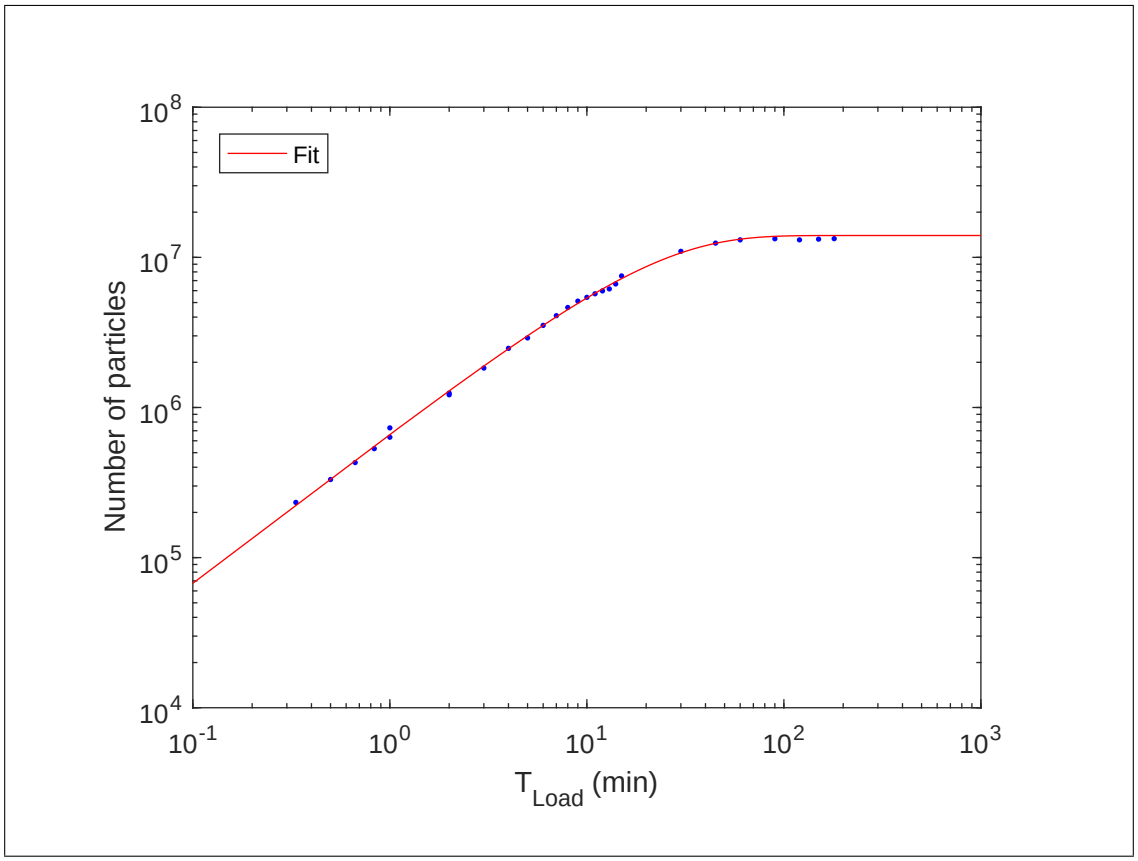

Figure 4.4: Number of particles N as a function of loading time t_{Load}. The red line represents the best fit of the function $N(t_{Load}) = N_0(1 - e^{-\frac{t_{Load}}{\tau_{Load}}})$ to the data.

Assuming that the rate $\mathrm{d}N_{Loss}/\mathrm{d}t = \frac{1}{\tau}\, N(t)$ at which trapped particles are lost is proportional to the number of trapped particles while the rate $\mathrm{d}N_{Loss}/\mathrm{d}t = \alpha\ I_{Beam}$ of newly trapped particles is proportional to the beam current I_{Beam}. In this case, the rate of change in number of trapped particles $\frac{\mathrm{d}N}{\mathrm{d}t}$ can be written as

$$\frac{\mathrm{d}N}{\mathrm{d}t} = \frac{\mathrm{d}N_{trap}}{\mathrm{d}t} - \frac{\mathrm{d}N_{Loss}}{\mathrm{d}t} = \frac{1}{\tau}\left[N_\infty - N(t)\right] \qquad \text{with } N_\infty = \alpha\tau I_{Beam}. \tag{4.2}$$

We determined the maximum number of particles N_∞ that can be simultaneously stored in the trap by fitting the solution to equation 4.2

$$N(t_{Load}) = N_\infty(1 - e^{-\frac{t_{Load}}{\tau_{Load}}}) \tag{4.3}$$

to the data, assuming that the trap is initially empty. The parameters fitting the data best are $N_\infty = 1.40(2) \times 10^7$ and $\tau_{Load} = 20.7(4)$ min. Note that the fit assumes that no space charge is present as the τ_{Load} does not depend on the number of trapped particles. As the data supports this assumption, N_∞ can be increased by increasing the beam current.

4.3 Storage time

To determine the rate $\mathrm{d}N_{Loss}/\mathrm{d}t$ at which trapped ions are lost, we loaded the trap for 5 min and stored the trapped ions for different times t ranging from 1 min to 3 h. It was observed, that the number of ions decreases exponentially in time with two different time constants τ_{Cold} for storage times up to 4 min and τ_{Hot} for times greater than 4 min. We suspect that the particles have a high temperature after loading, leading to an increased loss rate due to evaporative cooling. After $\approx$ 4 min the particles seem to have thermalized with the environment. Figure 4.5 shows the number of stored ions N as a function of the storage time t for times up to 10 min.

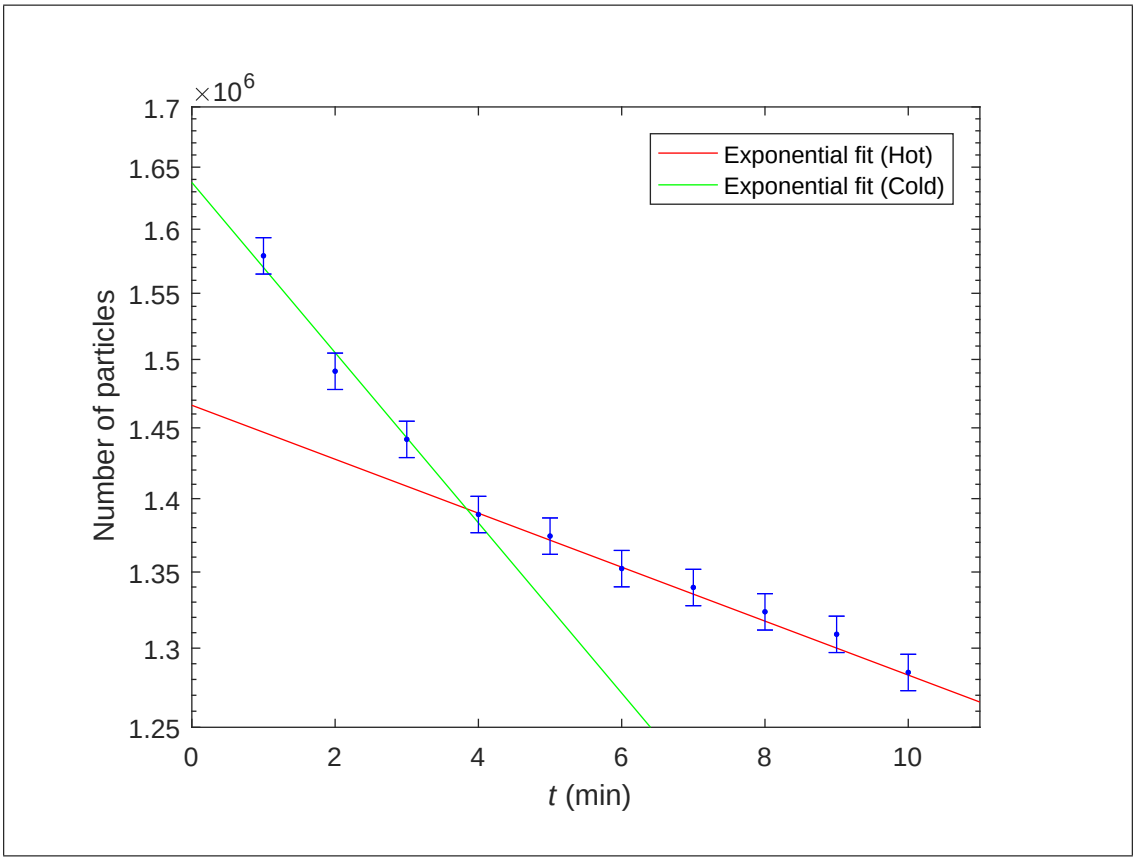

Figure 4.5: Number of particles N as a function of the storage time time t. Note that rate of particle loss is different for times below and above 4 min.

Fitting an exponential decay function

$$N(t) = N_0 e^{-\frac{t}{\tau}} \tag{4.4}$$

to the the data points above and below $t = 4$ min respectively, lets us determine the the parameters $N_{0,Hot}$, $N_{0,Cold}$, τ_{Hot} and τ_{Cold}. The fits yield the values $N_{0,Hot} = 1.64(2) \times 10^6$, $N_{0,Cold} = 1.476(9) \times 10^6$, $\tau_{Hot} = 23(3)$ min and $\tau_{Cold} = 75(2)$ min. Note that $N_{0,Cold}$ represents the initial number of particles if the ions were cold the whole time. As this assumption is violated, $N_{0,Cold}$ is different from $N_{0,Hot}$. We can approximate the cooling time t_{Cool} by determining at which time the number of particles predicted by the fit on the hot ions is equal to the number of particles predicted by the fit on the cold ones.

Inserting the values obtained from the fits into Eq. 4.4 and solving for t yields

$$t_{Cool} \approx \frac{\ln\left(\frac{N_{0,Cold}}{N_{0,Hot}}\right)}{\frac{1}{\tau_{Cool}} - \frac{1}{\tau_{Hot}}} \approx 3.8\,\text{min}. \tag{4.5}$$

Figure 4.6 depicts the number of particles for storage times up to 3 h. As the error bar are of similar size as the data marker, the error bars are not included the figure. It looks as if the loss rate decreased for storage times greater than 2 h but due to the large expenditure of time these measurements demand, there is too few data to make definitive claims.

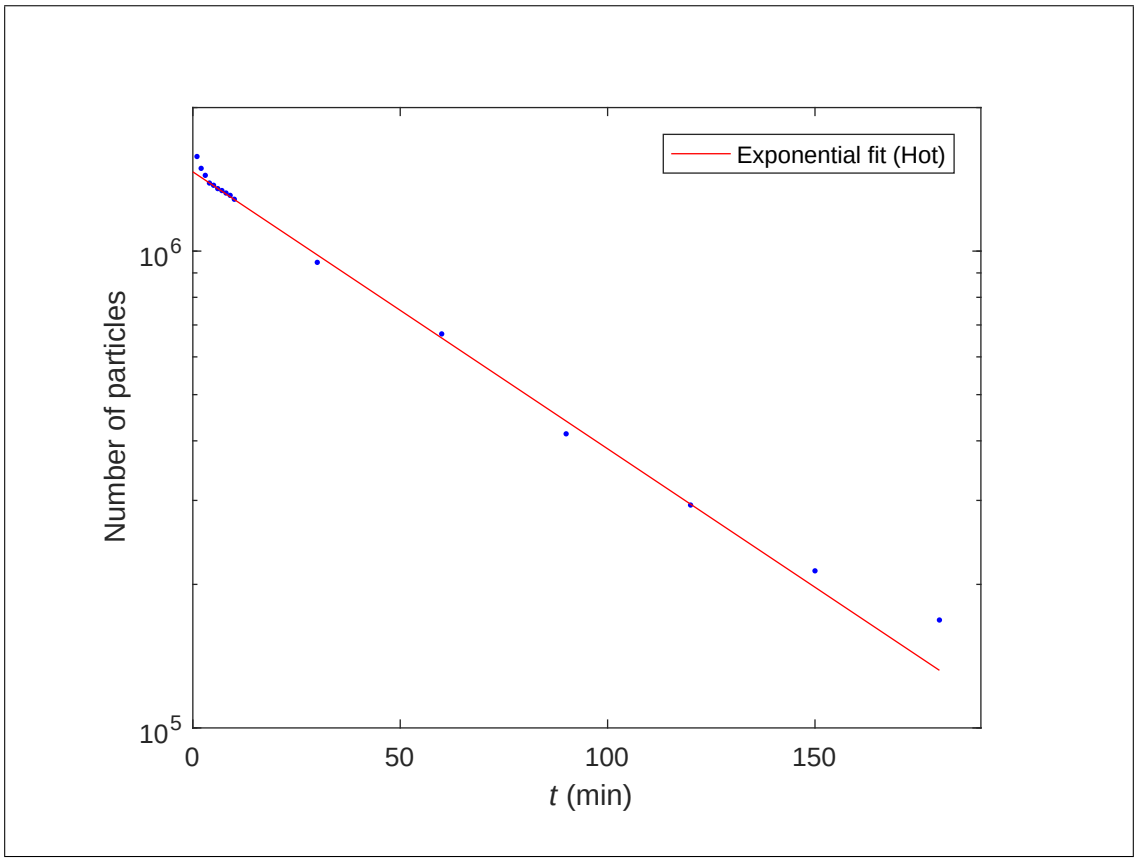

Figure 4.6: Number of particles N as a function of the storage time t up to 3 h.

4.4 Time of flight

To measure the ions' time of flight from the trap to the MCP as a function of the trapping time, the trap was loaded with ions for 30 s. After different trapping times t_{Trap}, the end cap on the back of the Paul trap was switched to a positive voltage, thus enabling the ions to leave the trap. The ions were accelerated by the bias voltage and hit the MCP located directly downstream of the Paul trap.

To reduce noise, the signal is by filtered by convolving it with a gaussian kernel of width $\sigma = 5\,\mu s$. Figure 4.7 shows a typical time of flight signal before and after this post-processing step.

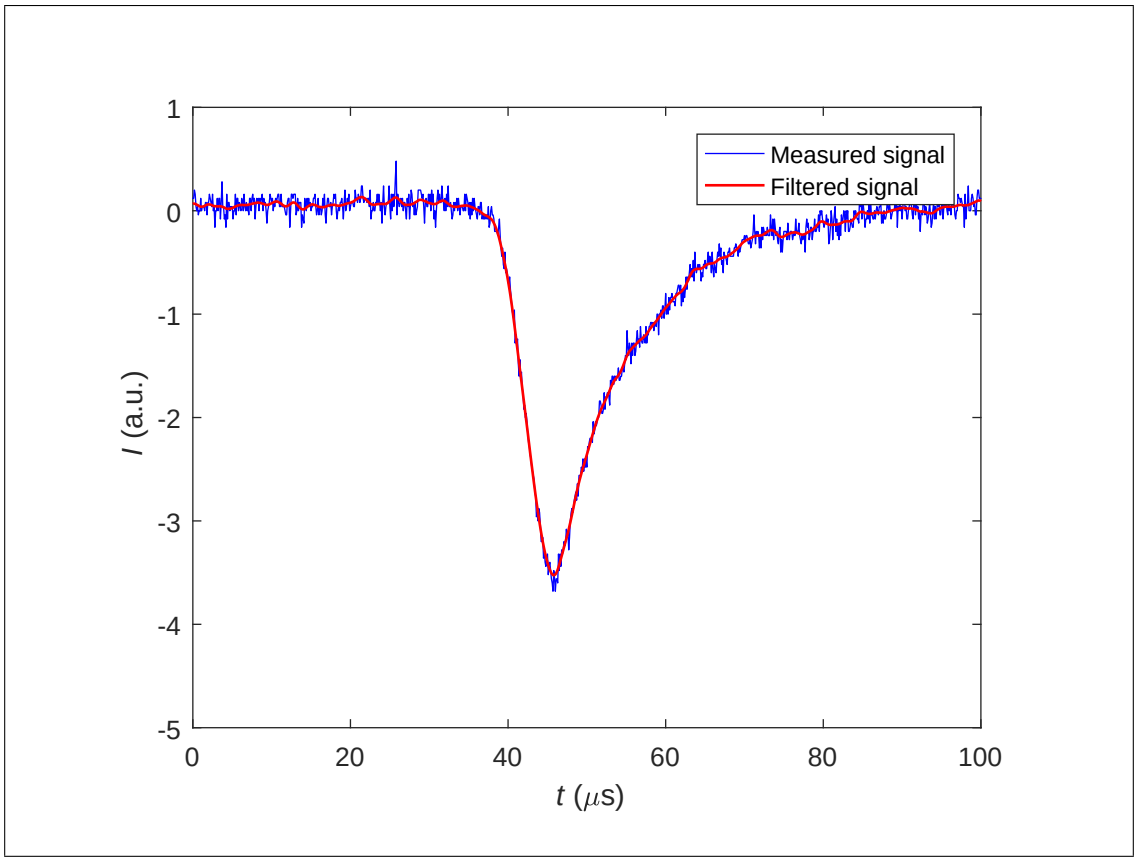

Figure 4.7: Voltage drop caused by the ions impinging on the MCP.

The time t_0 at which the fastest ions reach the MCP is approximated by fitting a straight line of the form

$$U(t) = a * (t - t_0) \tag{4.6}$$

to the falling edge of the noisy signal. To determine which data points correspond to the edge, the derivative is approximated by calculating the difference between the filtered signal at

times t_i and t_{i+1}. By excluding all points with a derivative greater than 20 % of the minimum derivative, the fit can be restricted to points lying on the falling edge. Figure 4.8 displays an example of this method, showing which points are excluded as well as the fit to the edge.

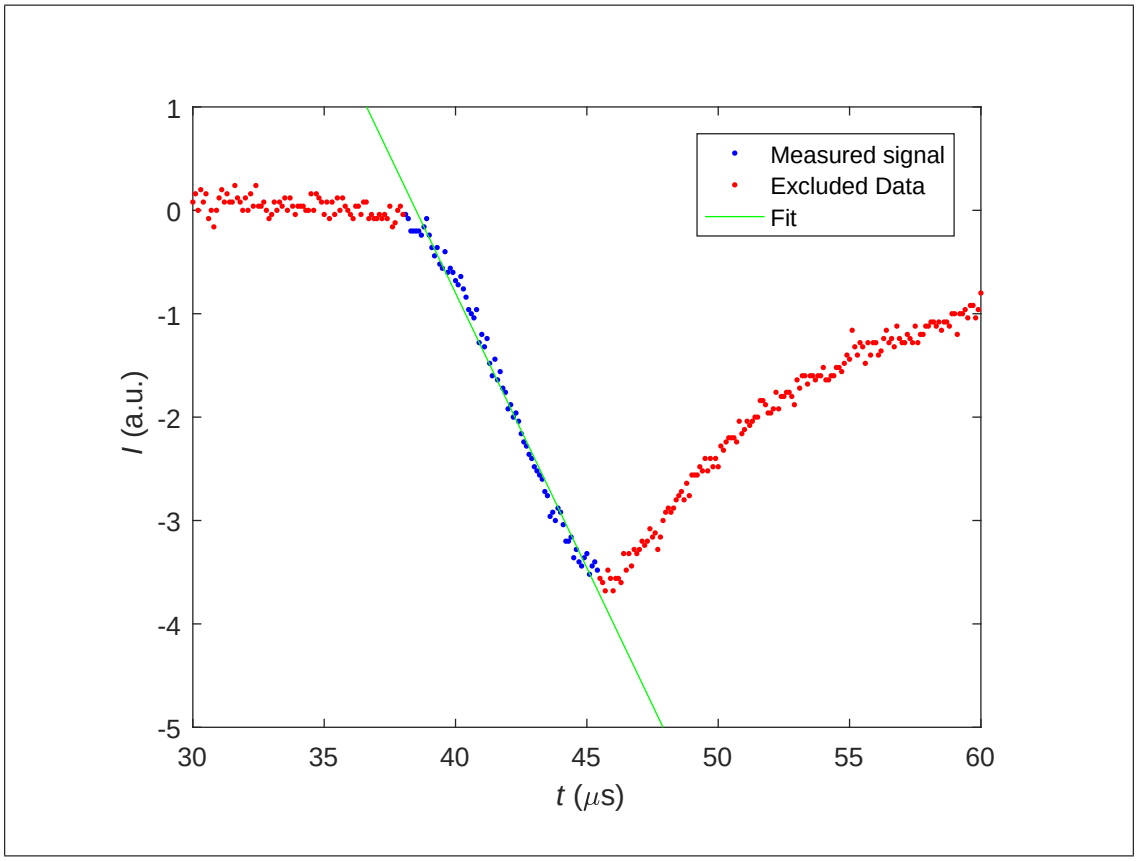

Figure 4.8: The fit is restricted to the falling edge by excluding points whose derivative is above 20 % of the minimum derivative.

By trapping the ions for different amounts of time, we investigated how the time of flight changes as the particles cool down. Figure 4.9 shows the time of flight t_0 of the fastest ions as a function of the trapping time t_{Trap}. As the MCP is located directly behind the trap, the time difference t_0 between opening the trap and registering the first ions is dominated by the systematic difference in trigger timing between the switch and the oscilloscope and not the actual time of flight. The trapping time was varied between 10 s and 300 s with each measurement repeated twice. The fact that the two series of measurements often do not agree within their margins of error suggests that the ejection voltage was not perfectly stable. Nevertheless, we can see that with increasing trapping time t_{Trap} the time-of-flight t_0 of the fastest ions increases as well. This observation is consistent with the fact that two different lifetimes were measured, suggesting that the particles are hot after loading and cool down over time. As the time of flight seems to stop increasing after between 3 min to 4 min the estimation of the cooling time $t_{Cool} \approx 3.8$ min is supported by the time-of-flight measurements.

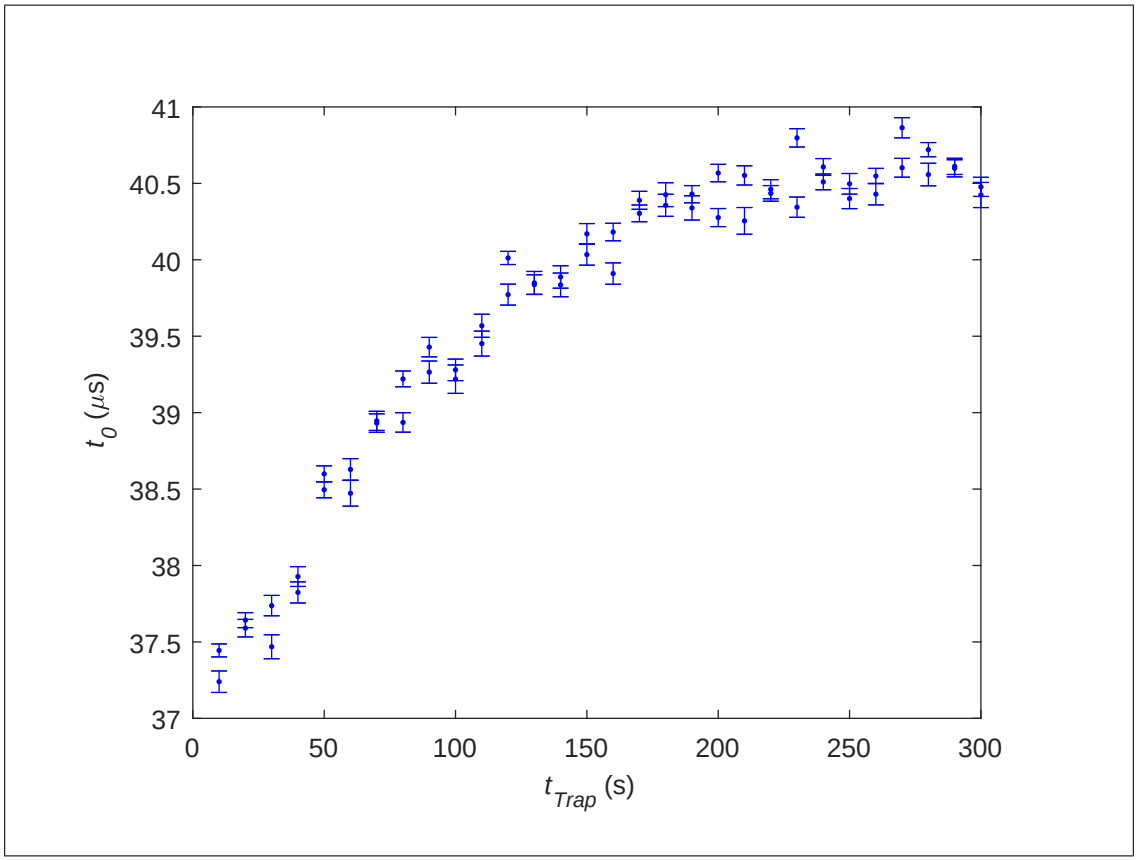

Figure 4.9: Time of flight t_0 as a function of the trapping time t_{Trap}. The time of flight of the fastest ions increases as the ions cool down.

4.5 Radial temperature

In addition to the measurements of the change in time of flight for different storage times, the shape of the ion cloud within the trap was imaged. Figure 4.10 shows the particle cloud after 10 s and 120 s storage time. As time progresses, the cloud shrinks in size while the particle density in the cloud center increases.

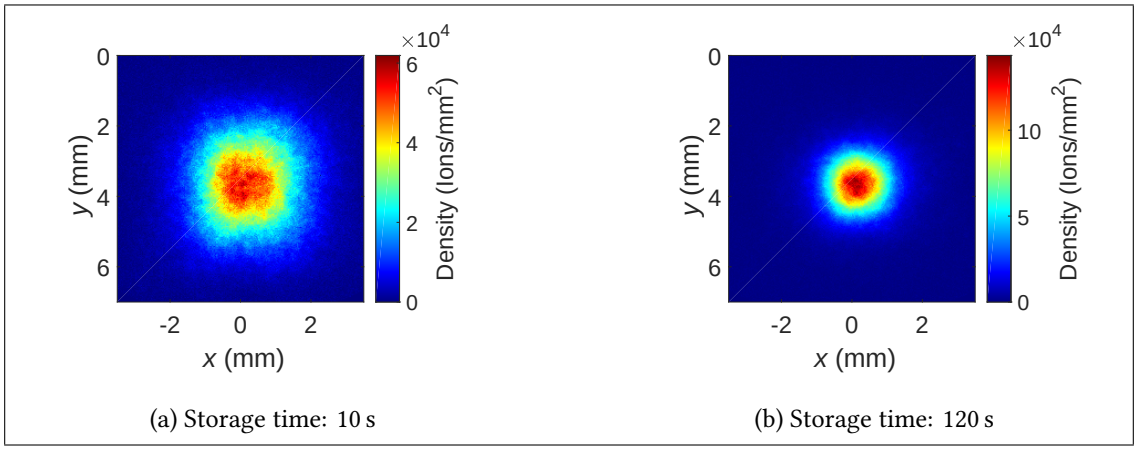

(a) Storage time: 10 s

(b) Storage time: 120 s

Figure 4.10: Particle density measured on the MCP after different storage times. Note the different color scales.

The ion density measured on the MCP can be approximated by a multivariate Gaussian distribution in x and y direction. Fitting the corresponding density function

$$I(x,y) = \frac{N}{2\pi\sigma_x\sigma_y} e^{-\frac{1}{2}\left(\frac{(x-x_0)^2}{\sigma_x^2}+\frac{(y-y_0)^2}{\sigma_y^2}\right)} \tag{4.7}$$

to the data allows us to determine the standard deviations in x and y direction. The quantity

$$r = \sqrt{\frac{\sigma_x^2+\sigma_y^2}{2}} \tag{4.8}$$

can be introduced as a characteristic radius which describes the radial cloud size. Figure 4.11 shows this radius r as a function of the storage time t_{Trap}. The error bars are too small to be depicted in the figure.

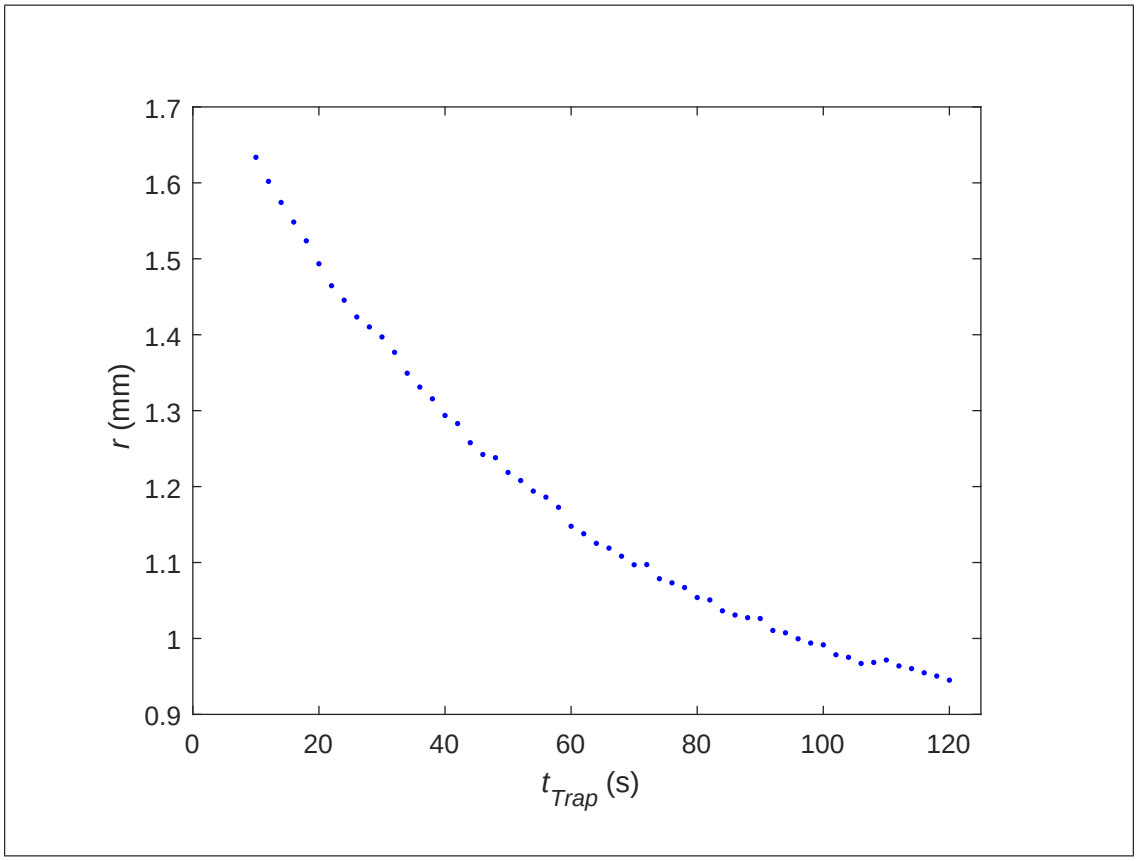

Figure 4.11: Radius r of the ion cloud as a function of the trapping time t_{Trap}.

As the trapping time increases, the cloud shrinks in size. At the same time, the total number N of trapped particles decreases. The particle density ρ in the ion cloud can be calculated by dividing the total number on ions N by the volume of the ion cloud. Assuming that the radial extension of the ion cloud's image corresponds to the radial extension in the trap, a rough estimate of the volume is given by the product of the area $A = \pi r^2$ covered by the cloud in radial direction and the distance $d = 99\,\text{mm}$ between the centers of the end cap electrodes. In this case, the ion density becomes:

$$\rho = \frac{N}{V} = \frac{N}{d\,\pi r^2}. \tag{4.9}$$

This approximation is valid if the distance between the end caps is large compared to the spacing between the rods, as in this case the field created by the end cap electrodes vanishes in the trap center and the radius of the cloud does not change significantly along the trap axis. Figure 4.11 depicts ρ as a function of the trapping time t_{Trap}. The error bars are too small to be shown in the same plot.

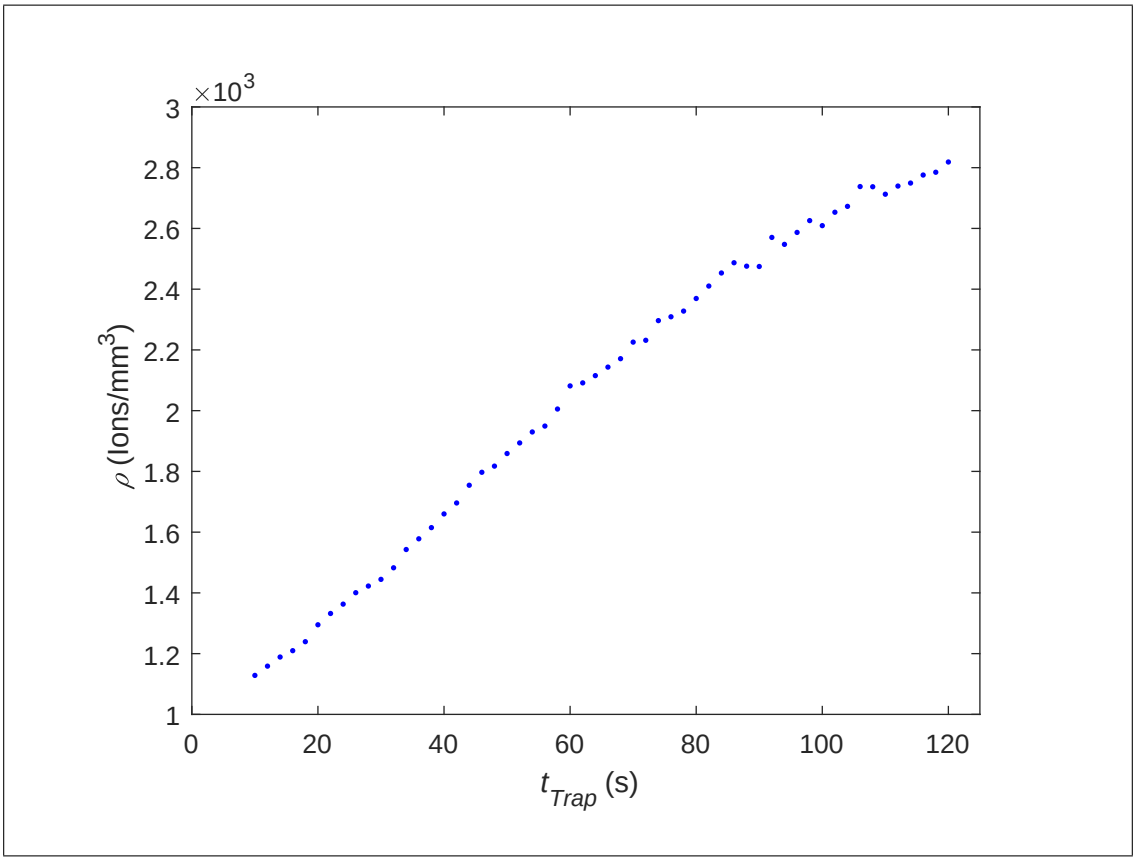

Figure 4.12: Particle density ρ in the center of the ion cloud as a function of the trapping time t_{Trap}.

With increasing time, the total number of trapped particles decreases, however, the ion density in the cloud increases.

To determine an estimate for the particle temperature T, we determine the effective potential $U_{Eff}(r)$ in radial direction created by the radio frequency. Using the adiabatic approximation given in Eq. 1.24, we can estimate the frequency ω of the macromotion driven by the applied radio frequency Ω_{RF} to be

$$\omega = \frac{\sqrt{a + \frac{q^2}{2}}}{2}\Omega_{RF}. \tag{4.10}$$

Since the distance between the end caps is long compared to the radial spacing between the rods, we can neglect a and obtain

$$\omega = \frac{q}{\sqrt{8}}\Omega_{RF}. \tag{4.11}$$

If more than one ion is trapped, ω is shifted by space charge effects. If we treat the ion cloud

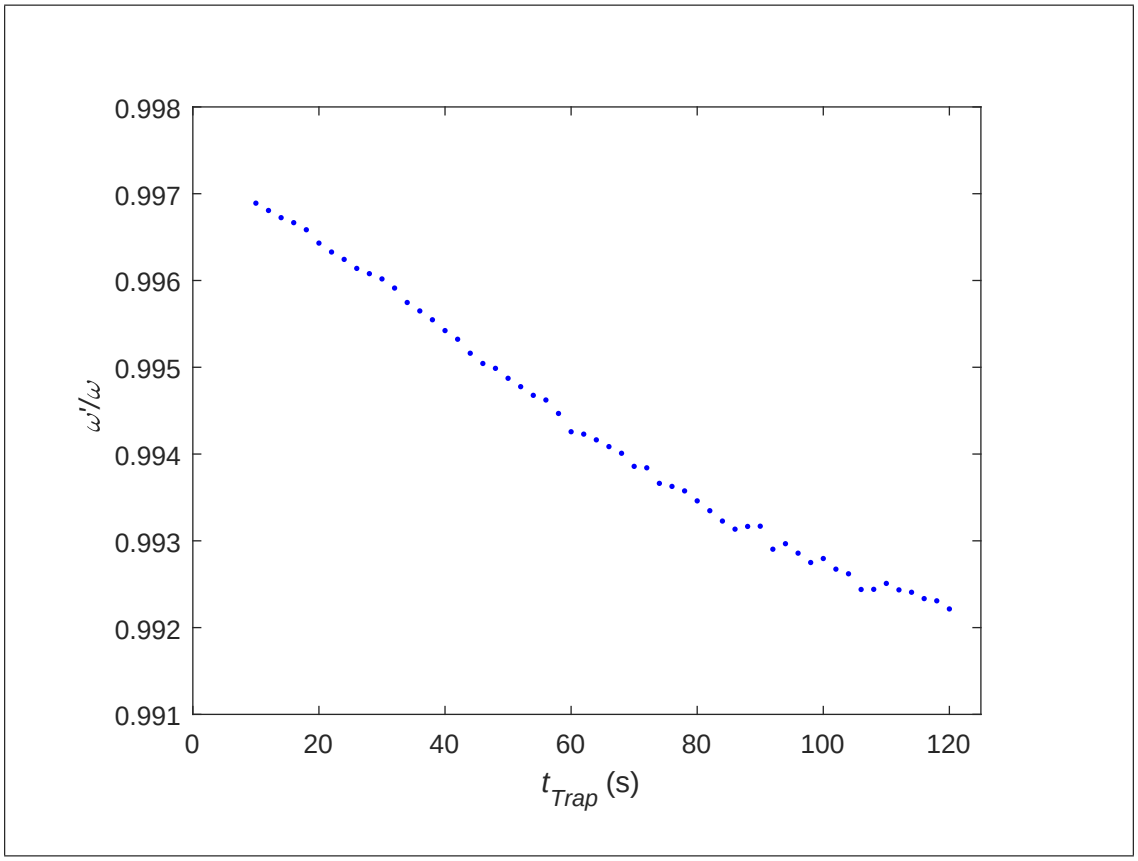

Figure 4.13: Ratio $\frac{\omega'}{\omega}$ for different trapping times t

as a homogeneously charged cylinder with charge density ρ, the potential within the cloud increases quadratically in radial direction. According to [41] in this case, the shifted frequency ω' is given by

$$\omega' = \omega\sqrt{1 - \frac{\omega_p^2}{3\omega^2}} \qquad \text{with } \omega_p = \sqrt{\frac{Q^2\rho}{\epsilon_0 m}}. \tag{4.12}$$

ω_p is the plasma frequency of the ion cloud and depends on the particle density ρ. Figure 4.13 depicts the ratio $\frac{\omega'}{\omega}$ for the different trapping times.

As ω'/ω is always close to one, the contribution of the space charge to the effective potential E_{Eff} trapping the ions is small. In the adiabatic approximation, the potential $U_{Eff}(r) \propto r^2$ governing the macromotion is assumed to be harmonic, which allows us to determine the second derivative of the potential using the equation of motion for a harmonic oscillator

$$\ddot{r} = -\omega'^2 r = \frac{Q}{m}E(r). \tag{4.13}$$

Since the second derivative of U_{Eff} is constant and the electric field associated with the

pseudo-potential vanishes at $r = 0$, we can insert $E(r) = \mathrm{d}^2 U_{Eff}/\mathrm{d}r^2 r$ into eq. 4.13 and obtain

$$\frac{\mathrm{d}^2 U_{Eff}(r)}{\mathrm{d}r^2} = \frac{m\omega'^2}{Q} = \frac{mq^2\Omega_{RF}^2}{8Q} - \frac{m\omega_p^2}{3Q}. \tag{4.14}$$

Combining equations eqs. 3.3, 4.12 and 4.14 yields

$$\frac{\mathrm{d}^2 U_{eff}(r)}{\mathrm{d}r^2} = \frac{QU_{AC}^2}{2m\Omega_{RF}^2 r_0^4} - \frac{Q\rho}{3\epsilon_0}. \tag{4.15}$$

Integrating twice over r assuming that both the potential and the field vanish at $r = 0$ leads to the pseudo-potential

$$U_{Eff}(r) = \frac{QU_{AC}^2}{4m\Omega_{RF}^2 r_0^4} r^2 - \frac{Q\rho}{6\epsilon_0} r^2. \tag{4.16}$$

Inserting $Q = -e$, $U_{AC} \approx 1260\,\mathrm{V}$, $m = 197\,\mathrm{u}$, $\Omega_{RF} = 1.938\,\mathrm{MHz}$ and $r_0 = 7\,\mathrm{mm}$ allows us to estimate the kinetic energy an Au^- ion has to possess to reach a distance r from the trap axis.

Knowledge of the ions cloud's radius r allows us to estimate its temperature T. Using the relationship

$$E_{kin} = k_B\, T \tag{4.17}$$

we can assign each cloud a temperature. The hottest particles in the cloud possess a kinetic energy equal to potential energy $E_{Eff}(r) = Q * U_{Eff}(r)$ at the radius r. Combining Eqs. 4.16 and 4.17 we can determine the temperature as a function of the radius and obtain

$$T(r) = \frac{Q^2 U_{AC}^2}{4k_B m\Omega_{RF}^2 r_0^4} r^2 - \frac{Q^2\rho}{6k_B\epsilon_0} r^2. \tag{4.18}$$

Directly after loading, the ions are hot and have initial temperatures T_0 of about $20 \times 10^3\,\mathrm{K}$. Over time the particles cool down and the cloud size shrinks. Assuming the cooling rate $\mathrm{d}T/\mathrm{d}t$ is proportional to the difference between the cloud temperature $T(t)$ and its final temperature T_∞, we can fit a model of the form

$$T(t) = T_\infty + (T_0 - T_\infty) e^{-\frac{t}{\tau_{Cool}}} \tag{4.19}$$

to the data. Figure 4.14 depicts the cloud's temperature T as a function of the trapping time t_{Trap}. The parameters describing the fit best are $T_0 = 20\,013(69)\,\mathrm{K}$, $T_\infty = 4766(43)\,\mathrm{K}$ and $\tau_{Cool} = 41.6(4)\,\mathrm{s}$. The final temperature T_∞ determined by the fit is significantly higher than room temperature ($\approx 300\,\mathrm{K}$) which suggests, that the ions do not thermalize with the environment but are heated by the applied radio frequency. Note that this estimation of the temperature relies on the assumption that the image of the ion cloud on the MCP corresponds to the radial density in the trap. This is only given if the ions leave the trap so fast that their momentum distribution does not influence the image on the screen and that the cloud is not blown up by ion-ion interaction. As these assumptions are likely violated, the estimated temperatures should be viewed as upper bounds of the real temperature.

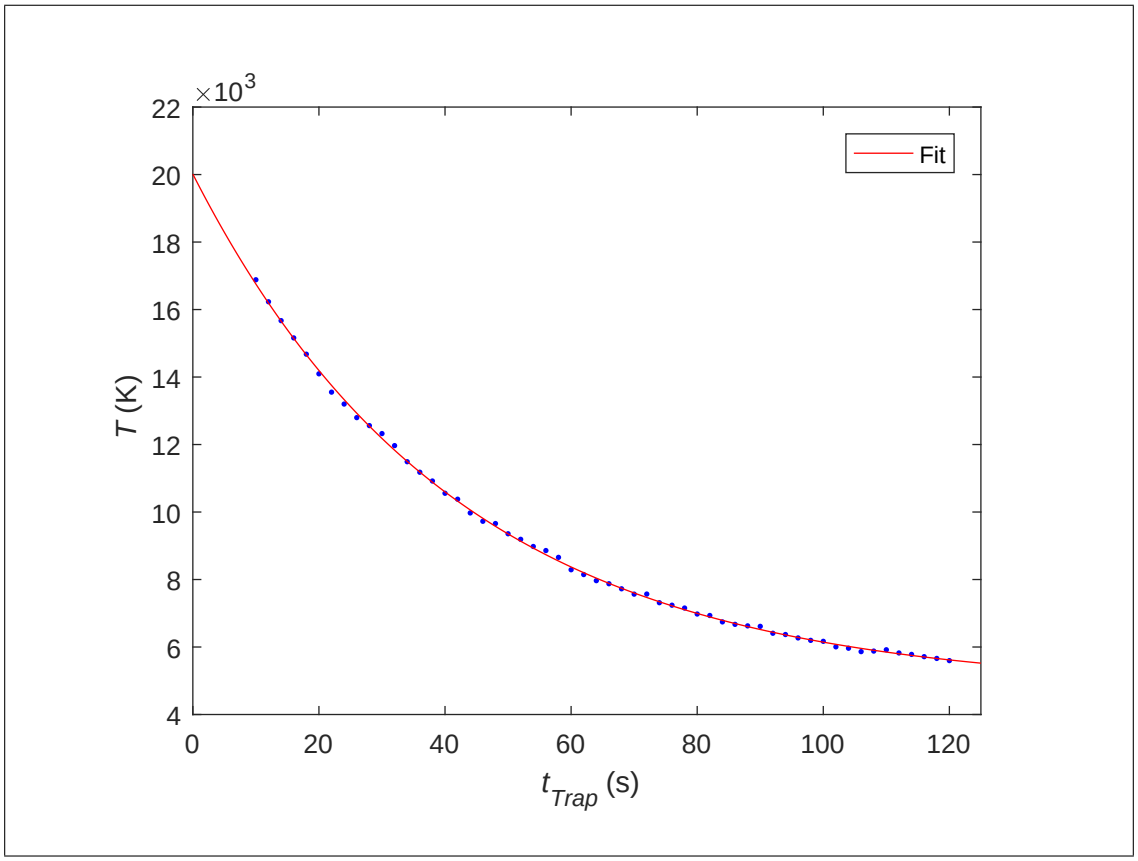

Figure 4.14: Temperature T of the ion cloud as a function of the trapping time t_{Trap}.

5 Summary and outlook

In the course of this thesis, the pre-existing design of a linear Paul trap was modified to allow trapping of negatively charged ions in a region free of strong magnetic fields. Two additional electrodes providing axial confinement were designed allowing rapid changes of the voltage on the end caps. The influence of these electrodes on the trapping potential was simulated, suggesting that the potential on the trap axis created by the end cap electrodes is equal to about 18 % of the potential applied to the electrodes. These simulations allowed the numerical calculation of a particle's motion in the trap. The trajectory was found to be stable despite the repelling force in radial direction created by the end caps. The current algorithm used to simulate the trajectory is a brute-force approach to the problem, as for each time step the electric field at the current particle location has to be interpolated. This interpolation takes a long time compared to the simple evaluation of a function. To increase the speed of the calculation of the electric field, other methods like a multipole expansion of the simulated potential can be applied. Implementing a faster way of calculating ion motions in the trap allows systematic simulations regarding trap depth and ion temperature. The current method also lacks the possibility to consider space charge effects and interactions between multiple ions trapped at the same time and should therefore be considered as an indicator that stable trapping can be achieved thanks to the new end cap electrodes.

The influence of a voltage applied to an end cap was determined experimentally by comparing the number of particles able to pass the trapping region for different voltages applied to the end cap. From these measurements it was determined that the potential on the trap axis created by the end cap electrodes is equal to $18.1(3)$ % of the voltage applied to the electrodes. This value agrees with the value obtained from the simulations. This suggests that the radio frequency confines the particles to areas close to the trap axis, as the potential created by the endcap electrodes decreases with the distance from the trap center in x direction.

The performance of the Paul trap was quantified using Au^- ions created in a Cs sputter source. Measurements of the loading time suggest that the maximum number N_∞ of gold ions that can simultaneously be trapped is on the order of $N_\infty \approx 14 \times 10^6$. The observation that the loading rate does not decrease at longer loading times suggests that N_∞ is not limited by space charge effects but rather by the lifetime of the particles in the trap and by the beam current. In case the beam current is increased in the future, the number of simultaneously trapped particles should increase as well. If the space charge in the trap can no longer be neglected two competing effects occur. On the one hand, a high space charge leads to an increase in the loss rate of trapped particles, as the repelling force between the ions acts against the confining force created by the pseudo-potential and the end caps. On the other hand, the presence of charged particles within the trap should increase the trapping rate for new particles as more collisions between

incoming and trapped ions increase the transfer of axial momentum to radial momentum.

Measurements of the ions' lifetime show that the rate at which ions are lost from the trap changes over time. This change in loss rate can be explained by the fact that the loading process heats up the ions. After loading is finished, evaporative cooling decreases the temperature of the ion cloud over a timespan of approximately 4 min. The lifetime of hot ions was determined to be $\tau_{Hot} = 23(3)$ min. This value is consistent with the time constant $\tau_{Load} = 20.7(4)$ min for the loading process, further indicating that loss rate of hot ions in the trap is the main factor limiting the loading process. After the particles have cooled down, their lifetime increases to $\tau_{Cold} = 75(2)$ min allowing detection of particles after multiple hours of storage.

The reduction in particle temperature is also noticeable as a change in time of flight. However, the difference in time between opening the trap and signal detection is dominated by systematic effects as the distance between the trap and the detector is small. Nevertheless the time of flight of the fastest particles increases with increasing trapping time, as the trapped particles cool down and lose kinetic energy over time. As the TOF signal is measured by discharging a capacitor, only the arrival time of the fastest ions can be detected accurately since the capacitor has to recharge before another voltage drop can be registered. To decrease the time constant for the recharge of the capacitor, the resistor over which the voltage drop is measured has to be decreased. This causes the amplitude of the signal to decrease as well. The decrease in amplitude can be counteracted by using a low-pass filter to remove high-frequency noise and amplifying the filtered signal before detection. Another way the TOF signal can be improved is by increasing the distance between the trap and the detector. As the imaging MCP has to be located as close as possible to the trap to create an accurate image of the ion cloud, there is a tradeoff between TOF and imaging measurements.

Measurements of the cloud size allow an estimation of the density of the trapped ions as well as their kinetic energy in radial direction and the associated temperature. With increasing trapping time, the hottest ions leave the trap, evaporatively cooling the remaining cloud. Despite the total number of ions decreasing, the ion density within the cloud increases. Using the adiabatic approximation, the effective potential U_{Eff} governing the ions' motion in radial direction was estimated. Knowledge of this potential allows the estimation of the ion cloud's temperature given its radius. It was found that the radial motion after loading corresponds to a temperature $T_0 \approx 20\,000$ K. The ions subsequently cool down to their final temperature T_∞ which was determined to be $T_\infty \approx 5000$ K. The time constant associated with this cooling process was determined to be $\tau_{Cool} \approx 40$ s. As the calculated temperatures depend quadratically on the radial extension r of the ion cloud, the absolute values of T_0 and T_∞ vary depending on the definition of the radial scale r. The timescale on which the cooling takes place, however, does not. These measurements assume that the cloud size on the imaging MCP is equal to the cloud size in the Paul trap. This assumption is only valid if the time of flight from the trap to the imaging MCP is so short that the radial momentum the trapped particles possess does not have an influence on the image.

Summarizing the results mentioned above, we can conclude that the objective of trapping

negative ions in an environment free from strong magnetic fields has been reached. The trap provides ion confinement for several hours while allowing radial and axial optical access to the trapped particles. However, it should be noted that the trap was operated at high radio frequency voltages which results in strong ion confinement. To perform laser cooling on the trapped ions, the amplitude of the applied AC voltage might have to be decreased in order to lower the amplitude of the micromotion and the associated heating rate.

Bibliography

[1] T. Haberer, J. Debus, H. Eickhoff, O. Jäkel, D. Schulz-Ertner, and U. Weber, "The heidelberg ion therapy center", *Radiotherapy and Oncology*, vol. 73, S186–S190, 2004.

[2] S. Petrie and D. K. Bohme, "Ions in space", *Mass spectrometry reviews*, vol. 26, no. 2, pp. 258–280, 2007.

[3] H. Häffner, T. Beier, S. Djekić, N. Hermanspahn, H.-J. Kluge, W. Quint, S. Stahl, J. Verdú, T. Valenzuela, and G. Werth, "Double penning trap technique for precise g factor determinations in highly charged ions", *The European Physical Journal D-Atomic, Molecular, Optical and Plasma Physics*, vol. 22, no. 2, pp. 163–182, 2003.

[4] K. Chang, R. McKeown, R. Milner, and J. Labrenz, "Search for long-lived doubly charged negative atomic ions", *Physical Review A*, vol. 35, no. 9, p. 3949, 1987.

[5] A. Kellerbauer and J. Walz, "A novel cooling scheme for antiprotons", *New Journal of Physics*, vol. 8, 2006, ISSN: 13672630. DOI: 10.1088/1367-2630/8/3/045.

[6] M. Amoretti, C. Amsler, G. Bonomi, A. Bouchta, P. Bowe, C. Carraro, C. Cesar, M. Charlton, M. Collier, M. Doser, *et al.*, "Production and detection of cold antihydrogen atoms", *Nature*, vol. 419, no. 6906, pp. 456–459, 2002.

[7] P. Comini, P.-A. Hervieux, and F. Biraben, "H+ production from collisions between positronium and kev antiprotons for gbar", *Hyperfine Interactions*, vol. 228, no. 1-3, pp. 159–165, 2014.

[8] M. Doser, "AEgIS: an experiment to measure the gravitaional interaction between matter and antimatter", *Journal of Physics*, vol. 199, no. 1, p. 8, 2010, ISSN: 1742-6596. DOI: 10.1088/1742-6596/199/1/012009.

[9] T. Andersen, H. Haugen, and H. Hotop, "Binding energies in atomic negative ions: Iii", *Journal of Physical and Chemical Reference Data*, vol. 28, no. 6, pp. 1511–1533, 1999.

[10] L. Pan and D. R. Beck, "Candidates for laser cooling of atomic anions: La- versus os-", *Physical Review A*, vol. 82, no. 1, p. 014 501, 2010.

[11] J. E. Jordan, "High-resolution doppler laser spectroscopy of the laser cooling candidate la^-", PhD thesis, 2015.

[12] R. C. Bilodeau and H. K. Haugen, "Experimental studies of os-: Observation of a bound-bound electric dipole transition in an atomic negative ion", *Physical review letters*, vol. 85, no. 3, p. 534, 2000.

[13] U. Warring, M. Amoretti, C. Canali, A. Fischer, R. Heyne, J. O. Meier, C. Morhard, and A. Kellerbauer, "High-resolution laser spectroscopy on the negative osmium ion", *Physical Review Letters*, vol. 102, no. 4, pp. 1–4, 2009, ISSN: 00319007. DOI: 10.1103/PhysRevLett.102.043001.

[14] C. Walter, N. Gibson, Y.-G. Li, D. Matyas, R. Alton, S. Lou, R. Field III, D. Hanstorp, L. Pan, and D. R. Beck, "Experimental and theoretical study of bound and quasibound states of ce-", *Physical Review A*, vol. 84, no. 3, p. 032 514, 2011.

[15] S. Vosko, J. Lagowski, I. Mayer, and J. Chevary, "Theoretical study of even-and odd-parity states in la- and ac-: Evidence for the uniqueness of la-", *Physical Review A*, vol. 43, no. 11, p. 6389, 1991.

[16] A. Covington, D. Calabrese, J. Thompson, and T. Kvale, "Measurement of the electron affinity of lanthanum", *Journal of Physics B: Atomic, Molecular and Optical Physics*, vol. 31, no. 20, p. L855, 1998.

[17] S. M. O'Malley and D. R. Beck, "Lifetimes and branching ratios of excited states in La-, Os -, Lu-, Lr-, and Pr-", *Physical Review A - Atomic, Molecular, and Optical Physics*, vol. 81, no. 3, pp. 1–8, 2010, ISSN: 10502947. DOI: 10.1103/PhysRevA.81.032503.

[18] S. Earnshaw, "On the nature of the molecular forces which regulate the constitution of the luminiferous ether", *Trans. Camb. Phil. Soc*, vol. 7, pp. 97–112, 1842.

[19] F. M. Penning, "Die glimmentladung bei niedrigem druck zwischen koaxialen zylindern in einem axialen magnetfeld", *physica*, vol. 3, no. 9, pp. 873–894, 1936.

[20] L. S. Brown and G. Gabrielse, "Geonium theory: Physics of a single electron or ion in a \text{Penning} trap", *Rev. Mod. Phys.*, vol. 58, no. 1, pp. 233–311, 1986.

[21] F. G. Major, V. N. Gheorghe, and G. Werth, *Charged Particle Traps: Physics and Techniques of Charged Particle Field Confinement*. 2006, vol. 37, p. 368, ISBN: 3540265767. DOI: 10.1007/978-3-540-92261-2. arXiv: arXiv:1011.1669v3. [Online]. Available: http://books.google.com/books?id=E5NxU-0nf5oC%7B%5C&%7Dpgis=1.

[22] W. Paul and H. Steinwedel, "Notizen: Ein neues massenspektrometer ohne magnetfeld", *Zeitschrift für Naturforschung A*, vol. 8, no. 7, pp. 448–450, 1953.

[23] T. W. Hänsch and A. L. Schawlow, "Cooling of gases by laser radiation", *Optics Communications*, vol. 13, no. 1, pp. 68–69, 1975, ISSN: 00304018. DOI: 10.1016/0030-4018(75)90159-5.

[24] D. Wineland and H. Dehmelt, "Proposed 1014 delta upsilon less than upsilon laser fluorescence spectroscopy on t1+ mono-ion oscillator iii", in *Bulletin of the American Physical Society*, AMER INST PHYSICS CIRCULATION FULFILLMENT DIV, 500 SUNNYSIDE BLVD, WOODBURY, NY 11797-2999, vol. 20, 1975, p. 637.

[25] D. J. Wineland, R. E. Drullinger, and F. L. Walls, "Radiation-pressure cooling of bound resonant absorbers", *Physical Review Letters*, vol. 40, no. 25, pp. 1639–1642, 1978, ISSN: 00319007. DOI: 10.1103/PhysRevLett.40.1639. arXiv: arXiv:1011.1669v3.

[26] H. J. Metcalf and P. van der Straten, "Laser cooling and trapping of atoms", *JOSA B*, vol. 20, no. 5, pp. 887–908, 2003.

[27] C. Adams and E. Riis, "Laser cooling and trapping of neutral atoms", *Progress in quantum electronics*, vol. 21, no. 1, pp. 1–79, 1997.

[28] V. Balykin, V. Letokhov, and V. Mushin, "Observation of the cooling of free sodium atoms in a resonance laser field with a scanning frequency", *JETP lett*, vol. 29, no. 10, pp. 560–564, 1979.

[29] W. Phillips, "Proposal to the office of naval research from the national bureau of standards", *Laser cooling and trapping of neutral atoms*, 1979.

[30] V. Letokhov, V. Minogin, and B. Pavlik, "Cooling and capture of atoms and molecules by a resonant light field", *Soviet Journal of Experimental and Theoretical Physics*, vol. 45, p. 698, 1977.

[31] W. Demtröder, *Experimentalphysik*. Springer, 2016, vol. 3.

[32] P. D. Lett, R. N. Watts, C. I. Westbrook, W. D. Phillips, P. L. Gould, and H. J. Metcalf, "Observation of atoms laser cooled below the doppler limit", *Physical Review Letters*, vol. 61, no. 2, p. 169, 1988.

[33] A. Aspect, E. Arimondo, R. e. a. Kaiser, N. Vansteenkiste, and C. Cohen-Tannoudji, "Laser cooling below the one-photon recoil energy by velocity-selective coherent population trapping", *Physical Review Letters*, vol. 61, no. 7, p. 826, 1988.

[34] R. Middleton, "A versatile high intensity negative ion source", *Nuclear Instruments and Methods In Physics Research*, vol. 214, no. 2-3, pp. 139–150, 1983, ISSN: 01675087. DOI: 10.1016/0167-5087(83)90580-X.

[35] H. B. Michaelson, "The work function of the elements and its periodicity", *Journal of Applied Physics*, vol. 48, no. 11, pp. 4729–4733, 1977, ISSN: 00218979. DOI: 10.1063/1.323539. arXiv: arXiv:1011.1669v3.

[36] R. Middleton, "A Negative-Ion Cookbook", vol. 1989, no. October 1989, pp. 1–194, 1990.

[37] C. König, "Trapping of negative gold ions in a penning trap", 2016.

[38] M. Drewsen and a. Brøner, "Harmonic linear Paul trap: Stability diagram and effective potentials", *Physical Review A*, vol. 62, no. 4, pp. 1–4, 2000, ISSN: 1050-2947. DOI: 10.1103/PhysRevA.62.045401.

[39] J. Pedregosa, C. Champenois, M. Houssin, and M. Knoop, "Anharmonic contributions in real RF linear quadrupole traps", *International Journal of Mass Spectrometry*, vol. 290, no. 2-3, pp. 100–105, 2010, ISSN: 13873806. DOI: 10.1016/j.ijms.2009.12.009. arXiv: 1001.1403. [Online]. Available: http://dx.doi.org/10.1016/j.ijms.2009.12.009.

[40] L. F. Shampine and M. W. Reichelt, "The MATLAB ODE Suite", *SIAM Journal on Scientific Computing*, vol. 18, no. 1, pp. 1–22, 1997, ISSN: 1064-8275. DOI: 10.1137/S1064827594276424. [Online]. Available: http://epubs.siam.org/doi/10.1137/S1064827594276424.

[41] J. Yu, M. Desaintfuscien, and F. Plumelle, "Ion density limitation in a Penning trap due to the combined effect of asymmetry and space charge", *Applied Physics B Photophysics and Laser Chemistry*, vol. 48, no. 1, pp. 51–54, 1989, ISSN: 07217269. DOI: 10.1007/BF00694417.

Erklärung:

Ich versichere, dass ich diese Arbeit selbstständig verfasst habe und keine anderen als die angegebenen Quellen und Hilfsmittel benutzt habe.

Heidelberg, den 1.6.2017 .....

Acknowledgements

First I would like to thank Priv.-Doz. Dr. Alban Kellerbauer for giving me the opportunity to conduct this thesis in his group. Working with you was always a pleasure as your calm and collected nature enables people to do their best. Without your continuing support and vast knowledge of the technical intricacies of running an experiment, this project would not have been successful.

My thanks go to the former and current members of the UNIC team located in Heidelberg: Dr. Elena Jordan, Charlotte König, Dr. Pauline Yzombard and Giovanni Cerchiari. Thank you for the fun and thoughtful conversations we shared at lunch and in the office. Apart from the people working in our group, I would like to thank all other colleagues at the Max Planck Institute for Nuclear Physics. Everybody I had contact with always did their best to provide an environment in which people can excel. Special thanks go to Mr. Gahn who provided me with the images of the setup.

I would like to thank my family for supporting me and providing a refuge in stressful times. It is always a pleasure to come home and spend time with you. Additional thanks go to my friends in Heidelberg and Esslingen who I shamefully neglected during the past two months. I would like to use this opportunity to once again thank Giovanni Cerchiari who I do not only consider as a colleague but as a friend. Thank you for your friendship, the Italian curse words you taught me and the support you provided me with. I will never forget the paragliding trips we shared and I am confident that there will be more to come.